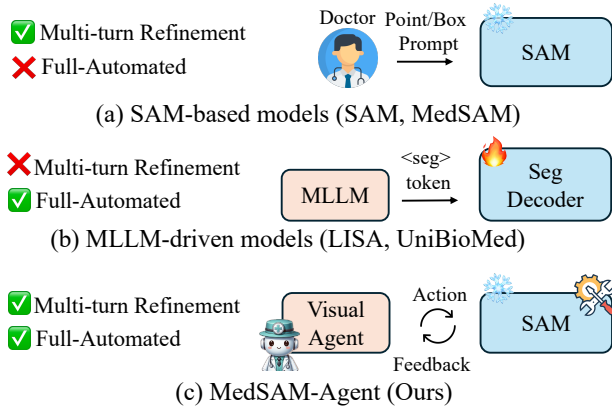


Shengyuan Liu<sup>1</sup> Liuxin Bao<sup>1</sup> Qi Yang<sup>2,3</sup> Wanting Geng<sup>2,4</sup> Boyun Zheng<sup>1</sup>  
Chenxin Li<sup>1</sup> Wenting Chen<sup>5</sup> Houwen Peng<sup>2,†</sup> Yixuan Yuan<sup>1,†</sup>

## Abstract

Medical image segmentation is evolving from task-specific models toward generalizable frameworks. Recent research leverages Multi-modal Large Language Models (MLLMs) as autonomous agents, employing reinforcement learning with verifiable reward (RLVR) to orchestrate specialized tools like the Segment Anything Model (SAM). However, these approaches often rely on single-turn, rigid interaction strategies and lack process-level supervision during training, which hinders their ability to fully exploit the dynamic potential of interactive tools and leads to redundant actions. To bridge this gap, we propose MedSAM-Agent, a framework that reformulates interactive segmentation as a multi-step autonomous decision-making process. First, we introduce a hybrid prompting strategy for expert-curated trajectory generation, enabling the model to internalize human-like decision heuristics and adaptive refinement strategies. Furthermore, we develop a two-stage training pipeline that integrates multi-turn, end-to-end outcome verification with a clinical-fidelity process reward design to promote interaction parsimony and decision efficiency. Extensive experiments across 6 medical modalities and 21 datasets demonstrate that MedSAM-Agent achieves state-of-the-art performance, effectively unifying autonomous medical reasoning with robust, iterative optimization. Code is available [here](#).



*Figure 1.* Comparison of medical image segmentation paradigms. (a) SAM-based models (e.g., SAM, MedSAM) require continuous manual prompting via points or bounding boxes. (b) MLLM-driven models (e.g., LISA, UniBioMed) employs MLLM with specialized seg decoders and <seg> tokens. (c) Ours MedSAM-Agent functions as an autonomous visual agent that performs multi-turn refinement through iterative feedback and tool interaction, emulating the professional decision-making process.

## 1. Introduction

Medical image segmentation stands as a foundational task in clinical computer vision, underpinning critical applications such as early disease diagnosis, surgical planning, and treatment response assessment. Traditional AI-driven segmentation approaches, including UNet (Ronneberger et al., 2015) and its variants (Chen et al., 2021; Isensee et al., 2021; Li et al., 2025a; Zhou et al., 2018), have demonstrated impressive performance in medical segmentation scenarios. However, these methods are primarily tailored to specific tasks or imaging modalities, posing significant challenges when generalizing to new tasks that were not encountered during model training. The emergence of the Segment Anything Model (SAM) (Kirillov et al., 2023; Ravi et al., 2024) represented a pivotal breakthrough, enabling high-quality segmentation through interactive human prompts (e.g., points, bounding boxes, or masks) (Ma et al., 2024; Wei et al., 2024b; Konwer et al., 2025; Ma et al., 2025b; Wu et al., 2025a; Gong et al., 2024). Nevertheless,

<sup>1</sup>Chinese University of Hong Kong, Hong Kong SAR, China

<sup>2</sup>Hunyuan Group, Tencent <sup>3</sup>Institute of Automation, the Chinese

Academy of Sciences, Beijing, China <sup>4</sup>Dalian University of Tech-

nology, Dalian, China <sup>5</sup>Stanford University, Stanford, USA. Corre-

spondence to: Yixuan Yuan <yxyuan@ee.cuhk.edu.hk>, Houwen Peng <henryllpeng@tencent.com>.

these SAM-derived interactive models remain inherently dependent on expert prompting (Fig. 1a), which prevents them from achieving autonomous, generalized segmentation without manual intervention.

Meanwhile, Multi-modal Large Language Models (MLLMs) (Sellergren et al., 2025; Xu et al., 2025b; Jiang et al., 2025a; Chen et al., 2024a) have shown remarkable perception and reasoning abilities in the medical domain, especially in visual question answering (Hu et al., 2024; Ye et al., 2024; Liu et al., 2021; Lau et al., 2018; He et al., 2020; Liu et al., 2025a) and report generation (Li et al., 2025b; Zambrano Chaves et al., 2025; Ma et al., 2025a; Chen et al., 2024b; Ru et al., 2026) tasks. While early attempts (Wu et al., 2025b; Huang et al., 2025b; Wang et al., 2025a) integrate MLLMs for segmentation via implicit tokens and additional pixel decoders (Fig. 1b), these methods often compromise semantic generalization by altering the original output space and shifting away from language-based outputs. Recent advancements (Li et al., 2024; Nath et al., 2025; Fathi et al., 2025) have shifted toward employing MLLMs as agents for invoking SAM tools, utilizing Reinforcement Learning from Verifiable Rewards (RLVR) during the post-training stage to integrate the high-level reasoning of MLLMs with the robust interactive segmentation of SAM by internalizing the autonomous tool-using.

However, existing methods still suffer from two major limitations: First, interaction strategies remain simplistic and inefficient. Current studies either rely on single-turn prompts (You & Wu, 2025; Liu et al., 2025b; Huang et al., 2025a; Li et al., 2024), treating SAM as a static segmentor rather than an iterative agent, or adhere to rigid, point-only trajectories (Zhu et al., 2025; Jiang et al., 2026). These point-centric paradigms lack the spatial flexibility to adaptively encompass morphological heterogeneity. In voluminous or ambiguously bounded cases, such methods fail to leverage bounding boxes as a human-like anchor for global context, leading to suboptimal step-wise refinement and under-utilized iterative potential. Second, the reinforcement learning process lacks process-level supervision. Existing RLVR frameworks (You & Wu, 2025; Huang et al., 2025a; Liu et al., 2025b; Jiang et al., 2025b; Liu et al., 2025c; Su et al., 2025a) focus predominantly on terminal outcomes, such as the final segmentation accuracy (e.g., Dice or IoU), while neglecting the efficiency and logical coherence of intermediate actions. Without specific rewards to incentivize action parsimony and per-step effectiveness, the agent may take unnecessary steps that do not contribute to mask refinement, which ultimately compromises both training convergence efficiency and final inference performance.

To address these limitations, we propose MedSAM-Agent, a framework that enables MLLMs to emulate human anno-

tators by treating the use of interactive segmentation tools as a multi-step decision-making process (Fig. 1c). First, we implement a hybrid prompting strategy to generate diverse, high-quality expert trajectories, enabling the model to internalize human-like decision heuristics and adaptive refinement strategies by boxes and points. Then we develop a two-stage training pipeline that integrates multi-turn, end-to-end outcome verification with a clinical-fidelity process reward design to promote interaction parsimony and decision efficiency. This framework jointly optimizes for segmentation accuracy and procedural efficiency, ensuring the agent learns to make precise, non-redundant decisions. Consequently, MedSAM-Agent achieves state-of-the-art performance across 6 medical modalities and 21 datasets, demonstrating exceptional cross-modal generalization and tool-use versatility. Our key contributions are summarized as follows:

- We introduce the MedSAM-Agent framework, which reformulates medical image segmentation by transitioning from static pixel-wise classification to a dynamic decision-making paradigm.
- We develop a hybrid prompting strategy for expert-curated trajectory generation, followed by a two-stage training pipeline optimized via a clinical-fidelity process reward design.
- We conduct comprehensive experiments across 6 medical modalities that demonstrate superior segmentation performance and robust tool-agnostic generalization.

## 2. Related Works

### 2.1. Medical Image Segmentation

Traditional medical image segmentation methods like UNet (Ronneberger et al., 2015), nn-UNet (Isensee et al., 2021), and other representative architectures (Li et al., 2025a; Zhou et al., 2018; Chen et al., 2021; Fan et al., 2020) are inherently task-specific, which require dedicated training for each individual segmentation task, thus exhibiting limited generalization across diverse medical imaging scenarios (Butoi et al., 2023; Ye et al., 2023). The advent of the SAM (Kirillov et al., 2023; Ravi et al., 2024) has sparked renewed hope for achieving generalizable medical image segmentation. Consequently, numerous SAM-derived models (Ma et al., 2024; Wei et al., 2024b; Konwer et al., 2025; Zhang et al., 2025c; Ma et al., 2025b; Wu et al., 2025a; Wang et al., 2024; Zhao et al., 2025) have been fine-tuned on large-scale medical image datasets. However, these interactive segmentation models typically rely on explicit human-provided prompts (e.g., points, boxes, or masks) to guide the segmentation process, limiting their autonomy. Parallel to this, the advancement of MLLMs has enabled text-guided medical image segmentation (Huang et al., 2025b; Wang et al.,

2025b; Ning et al., 2025), such as Citrus-V (Wang et al., 2025a) and UniBiomed (Wu et al., 2025b). Despite their flexibility in leveraging textual instructions, these MLLM-driven methods are constrained by the inherent limitations of MLLMs in capturing fine-grained pixel-level details, and they lack the iterative refinement capability that characterizes SAM-based interactive segmentation frameworks. In contrast, our proposed method addresses these gaps by mimicking the annotation trajectories of human experts through the integration of interactive segmentation tools, enabling both autonomous guidance and iterative optimization.

## 2.2. Reinforcement Learning in MLLM

Driven by the success of DeepSeek-R1 (Shao et al., 2024), reinforcement learning (RL) has fundamentally reshaped the training paradigms for large language models (Schulman et al., 2017; Yu et al., 2025; Zheng et al., 2025a; Zhang et al., 2020). Recent studies (Peng et al., 2025; Shen et al., 2025a; Feng et al., 2025; Liu et al., 2025d;b;d) have demonstrated that simple yet verifiable rewards can effectively extend a model’s reasoning capabilities from text-only tasks to multi-modal scenarios, a transition that has also proven effective in specialized medical tasks (Wang et al., 2025c; Lai et al., 2025b; Pan et al., 2025; Zhang et al., 2025b; Chen et al., 2025; Xu et al., 2025a). For fine-grained understanding tasks, milestone developments like OpenAI-o3 (OpenAI, 2025) have introduced the concept of “thinking with images”, leveraging iterative zoom-in mechanisms (Zheng et al., 2025b; Lai et al., 2025a; Shen et al., 2025b; Su et al., 2025a; Zhang et al., 2025d) or external tool invocation (Su et al., 2025b; Huang et al., 2025a; You & Wu, 2025; Wu et al., 2025c; Zhang et al., 2025a) to actively refine visual perception. In the medical domain, while similar efforts (Huang et al., 2025c; Yan et al., 2025; Li et al., 2024; Wang et al., 2025d) have attempted to integrate tool-use, existing medical MLLMs (Li et al., 2024; Jiang et al., 2026; 2025b) predominantly operate within a single-turn interaction paradigm or rely on monotonic clicking strategies that lack strategic diversity. Consequently, their potential to function as autonomous agents capable of dynamic, multi-step action planning remains underdeveloped.

## 3. Methods

### 3.1. Expert-Curated Trajectory Generation

Given an image  $I$  and a segmentation target prompt  $P$ , medical experts commonly employ interactive segmentation tools: based on the original image  $I$  and the real-time updated mask  $M$ , they iteratively provide positive click points (marking regions confirmed as the target) and negative click points (excluding non-target regions). This iterative interaction facilitates the efficient generation of high-quality masks that meet clinical annotation standards. We formalize this

procedure as a multi-step decision-making process. Given the prompt  $P$  and input image  $I$ , the policy model iteratively generates an action  $a_t$ . This action interacts with the environment by invoking the image segmentation tool, resulting in a new observation  $o_t$ . This observation is appended to the interaction history and fed back to the policy model  $\pi_\theta(a_t|s_t, I, P)$ . The components are detailed as follows:

**Action  $a_t$ :** To simulate expert behavior, we define the action space to encompass bounding box operations, point-wise clicks, and a stop signal. The box operation is represented as  $a_t = [x_1, y_1, x_2, y_2]$  to provide a global spatial prior, while a click operation consists of a coordinate  $a_t = [x_1, y_1]$  paired with an attribute  $\alpha \in \{+1, -1\}$  to denote positive or negative refinement; finally, the stop operation is triggered to terminate the sequence once the segmentation reaches the desired fidelity.

**Observation  $o_t$ :** In agentic RL, the observation  $o_t$  is obtained based on the parameters indicated by the corresponding action  $a_t$ . Concretely, it is the updated mask  $M_t$  predicted by the interactive segmentation network  $F_{seg}$ . Prior to the execution of a stop action, the interactive model maintains a record of all previous actions, with the updated mask computed as  $M_t = F_{seg}(I, o_{t-1}, a_t)$ , where  $M_t$  directly serves as  $o_t$ . These observation tokens are appended to the ongoing rollout sequence and fed back into the model as input for the subsequent step. When the action  $a_t = stop\_action$ , no tool invocation is performed; instead,  $o_t$  directly inherits the result from the previous iteration  $o_{t-1}$  and is output as the final predicted mask.

**State  $s_t$ :** At each step  $t$ , the state  $s_t$  is defined as:

$$s_t = \{(a_0, o_0), (a_1, o_1), \dots, (a_{t-1}, o_{t-1})\} \quad (1)$$

Given the state  $s_t$ , the action  $a_t \sim \pi_\theta(a | s_t)$  is sampled from the MLLM policy  $\pi_\theta$ , serving as the next input token. This long sequence continues to interleave until either the stop action is generated or the maximum number of tool calls is reached. The objective of our framework is to develop an MLLM capable of executing a segmentation policy  $\pi_\theta(a_t|s_t, I, P)$  that emulates the decision-making process of medical experts. To facilitate this, we construct a trajectory dataset  $D_{traj} = \{(I, M_{target}, P, s_t)\}$ , derived from an initial dataset  $D_{seg} = \{(I, M_{target}, P)\}$ .

**Hybrid Prompting Strategy.** While existing methods (Zhu et al., 2025; Jiang et al., 2026) rely on a rigid point-wise simulation driven by pixel-level discrepancies, they typically restrict the action space to sequential clicks. Such a limitation fails to capture the multi-modal nature of human workflows, where practitioners often initiate segmentation by defining an ROI. To bridge this gap, we propose a hybrid prompting strategy (Fig. 2) that offers greater spatial flexibility. This strategy incorporates both Box-to-Point and Sequential-Click paradigms to better mimic clinical

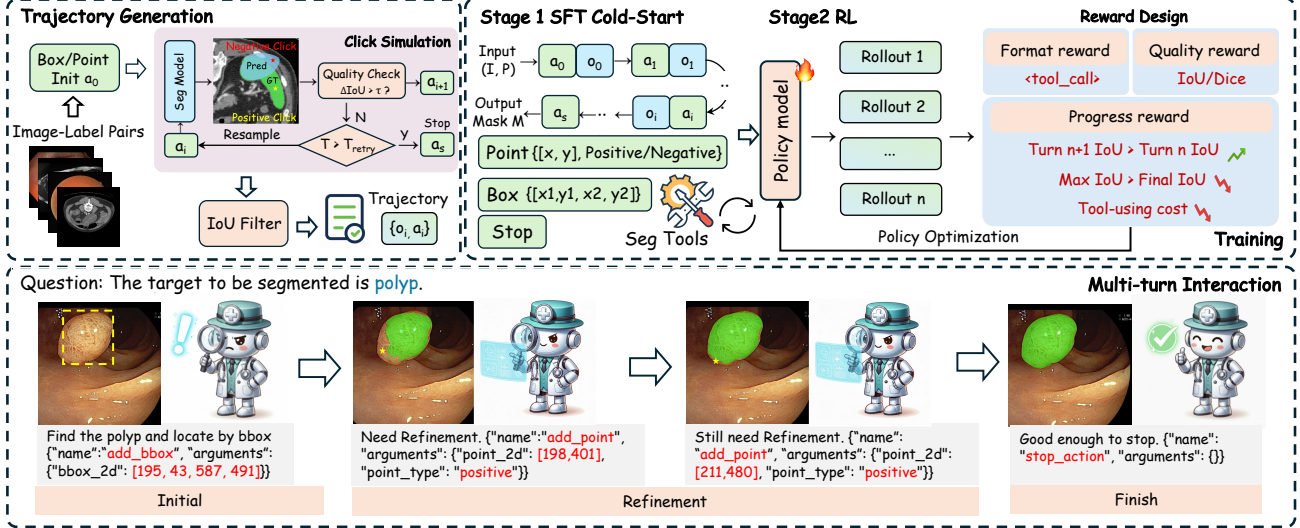


**Figure 2. Overview of MedSAM-Agent.** We develop a hybrid prompting strategy for expert-curated trajectory generation that transforms image-label pairs into high-quality interaction sequences via simulated clicks and IoU-based filtering. Then these trajectories support a two-stage training pipeline, stage-1 SFT cold-start for initial capability and stage-2 RL optimized by a fine-grained reward design. MedSAM-Agent can autonomously select between box and point tools and execute the “stop” action once the refinement is complete.

expertise. In the Box-to-Point workflow, the trajectory is initialized with a bounding box action generated by extracting the axis-aligned rectangle of  $M_{\text{target}}$  with a controllable random jitter to simulate human imprecision. For subsequent refinement, the agent identifies the most significant False Negative (FN) and False Positive (FP) components. By applying a distance transform to these error regions, corrective clicks are sampled at the centroids of the largest error clusters, ensuring each action addresses the most salient morphological defects.

To guarantee the quality and efficiency of the synthesized trajectories, we implement a progress-constrained sampling mechanism. We contend that an expert-level trajectory must consist of informative and effective actions; consequently, we enforce a constraint where each simulated action must yield an incremental IoU gain ( $\Delta\text{IoU}$ ) exceeding a predefined threshold  $\tau$ . To prevent the inclusion of sub-optimal or redundant interactions, a retry mechanism is introduced: if a candidate action fails to satisfy the progress threshold, the simulator performs iterative resampling up to  $N$  trials to identify a more constructive interaction. Following the generation of all sequences, a global IoU filter is applied to both paradigms to prune trajectories that fail to reach a target performance threshold. This validation process effectively filters out stochastic noise and ensures that  $D_{\text{traj}}$  is composed of high-quality, monotonically improving sequences, thereby providing a robust supervisory signal for policy optimization. By integrating these components, we successfully construct the expert-curated trajectories  $D_{\text{traj}}$ . The details of the trajectory generation algorithm are shown in the Appendix.

### 3.2. Two-stage Training Pipeline

Building upon these trajectories, we employ a two-stage training pipeline: Supervised Fine-Tuning (SFT) serves as the initial cold-start, followed by Reinforcement Learning with Verifiable Rewards (RLVR) in the second stage to further refine the agent’s decision-making policy. The overall training pipeline is shown in Fig. 2.

#### 3.2.1. SFT COLD-START

To bridge the gap between natural language reasoning and tool interaction, we format the trajectory data into a structured tool-calling schema. Each expert action  $a_t$  is converted into a specialized token sequence enclosed within  $\langle \text{tool\_call} \rangle$  tags, resulting in a SFT dataset  $D_{\text{SFT}}$  comprising 449K samples. The system prompt  $P$  encompasses a comprehensive description of the task requirements and action space, alongside a semantic definition of the target object. This design ensures the model maintains a global objective while grounding its actions in the specific visual and textual context of the segmentation target. The details of the prompt design are shown in the Appendix.

As each expert-curated action is tokenized into a discrete sequence, the model is trained to predict the next token in an auto-regressive manner. Formally, the optimization objective is defined by the following negative log-likelihood loss:

$$\mathcal{L}_{\text{SFT}}(\theta) = -\mathbb{E}_{(I, P, y) \sim D_{\text{SFT}}} \left[ \sum_{t=1}^{|y|} \log \pi_{\theta}(y_t | I, P, y_{<t}) \right] \quad (2)$$

where  $y$  denotes the target token sequence representing the expert trajectory  $s_T$ ,  $y_t$  is the  $t$ -th token of the sequence, and  $y_{<t}$  represents the preceding context including the image  $I$ , the text prompt  $P$ , and previously generated tokens. To provide the model with a precise perception of the current segmentation state, the mask generated at each step is overlaid on the original image  $I$  as a dedicated visual prompt, which is then re-encoded by the vision encoder to inform the subsequent action. This iterative visual feedback loop enables the agent to dynamically observe the refined boundaries and localize remaining errors throughout the trajectory.

This cold-start phase is foundational for the subsequent reinforcement learning stage; by minimizing the imitation loss, the model aligns its initial policy distribution with the decision-making heuristics of medical experts, effectively acquiring fundamental visual grounding capabilities. This strategic initialization ensures that the agent enters the reinforcement learning phase with a pre-established competency in autonomous tool invocation and spatial reasoning.

### 3.2.2. CLINICAL-FIDELITY PROCESS REWARD DESIGN

Unlike prior approaches (Liu et al., 2025b; Huang et al., 2025a; You & Wu, 2025) that predominantly rely on outcome-based rewards for single-pass predictions, we propose a multi-dimensional reward framework. This design meticulously balances final segmentation fidelity with the strategic efficiency of the interactive process, fostering a policy that is both accurate and resource-conscious.

**Format Reward ( $R_{fmt}$ ):** The format reward  $R_{fmt}$  is engineered to enforce adherence to the interactive protocol through a partial-credit mechanism. It rewards two fundamental behaviors: (1) the active deployment of interaction primitives (e.g., *add\_bbox* or *add\_point*) and (2) the execution of a definitive *stop\_action* to terminate the sequence. By assigning 0.5 points to each criterion, we prevent the model from collapsing into infinite loops, ensuring the agent learns the logical boundaries of task completion.

**Quality Reward ( $R_{qual}$ ):** The core objective is to maximize the final intersection between the predicted mask and the ground truth. We define the quality reward  $R_{qual}$  as a weighted ensemble of the IoU and the Dice Coefficient:

$$R_{qual} = w_{iou} \cdot \text{IoU}_{final} + w_{dice} \cdot \text{Dice}_{final} \quad (3)$$

$w_{iou}$  and  $w_{dice}$  are weighted hyper-parameters. While IoU provides a standard geometric consistency measure, the inclusion of the Dice coefficient is critical for medical contexts, as it offers higher sensitivity to small-scale lesions and anatomical structures, thereby mitigating the penalty variance in class-imbalanced scenarios.

To optimize the agent's decision-making trajectory, we in-

duce a process reward comprised of three distinct components designed to foster intelligent interaction logic:

**Progressive Improvement Bonus ( $R_{imp}$ ):** This component incentivizes the agent to achieve monotonic quality gains across iterations. By rewarding the cumulative positive deltas in IoU, we discourage redundant or ineffective interactions that fail to contribute to mask refinement.

$$R_{imp} = \sum_{t=1}^{N-1} \max(0, \text{IoU}_t - \text{IoU}_{t-1}) \quad (4)$$

**Overshoot Penalty ( $R_{over}$ ):** This penalty is designed to encourage efficient termination and prevent redundant interactions. Since the model lacks access to ground-truth IoU during inference, it must internalize the ability to decide when to conclude an interaction based solely on visual cues. By penalizing any quality degradation following the peak IoU ( $\text{IoU}_{max} - \text{IoU}_{final}$ ), during training,  $R_{over}$  effectively disciplines the agent to recognize the point of diminishing returns. This mechanism ensures the model learns an optimal stopping policy, minimizing unnecessary iterations and maximizing inference efficiency in real-world scenarios.

**Tool-cost Penalty ( $R_{cost}$ ):** Recognizing the computational cost of each interaction, we apply a linear penalty proportional to the sequence length. This encourages the policy to pursue the shortest path to high-fidelity segmentation, prioritizing efficiency without compromising terminal accuracy.

The terminal reward  $R_{total}$  for each output  $O_i$  is a composite metric that accounts for structural adherence, segmentation accuracy, and procedural efficiency:

$$R_{total} = w_1 \cdot R_{fmt} + w_2 \cdot \text{clip}(R_{qual} + \lambda_1 R_{imp} - \lambda_2 R_{over} - \lambda_3 R_{cost}, 0, 1) \quad (5)$$

where  $w$  and  $\lambda$  are weighted hyper-parameters,  $\text{clip}(\cdot, a, b)$  limits the input to the range  $[a, b]$ . To optimize the interactive policy, we employ Group Relative Policy Optimization (GRPO (Shao et al., 2024)). The objective function  $\mathcal{J}_{GRPO}(\theta)$  is defined by sampling a group of  $G$  rollouts  $\{O_1, O_2, \dots, O_G\}$  for each query  $q$ :

$$\mathcal{J}_{GRPO}(\theta) = \mathbb{E}_{q \sim \mathcal{D}, \{O_i\}_{i=1}^G \sim \pi_{\theta_{old}}} \left[ \frac{1}{G} \sum_{i=1}^G \min \left( \frac{\pi_{\theta}(O_i|q)}{\pi_{\theta_{old}}(O_i|q)} A_i, \text{clip} \left( \frac{\pi_{\theta}(O_i|q)}{\pi_{\theta_{old}}(O_i|q)}, 1 - \epsilon, 1 + \epsilon \right) A_i \right) \right] \quad (6)$$

where the advantage  $A_i$  is computed by normalizing the multi-component reward  $R_{total}$  within each group to capture the relative quality of the rollouts  $O_i$ :

$$A_i = \frac{R_{total,i} - \text{mean}(R_{total,1}, \dots, R_{total,G})}{\text{std}(R_{total,1}, \dots, R_{total,G})} \quad (7)$$

**Table 1. Quantitative comparison across six medical imaging modalities.** The results report the mean Dice and IoU scores for each specific modality and the overall average. **Point** and **Box** indicate the interactive prompts derived from ground-truth center points and bounding boxes, used to evaluate single-round segmentation performance. **Bold** and underlined values represent the best and second-best performance among non-interactive methods, respectively.

| Method                             | CT           |              | MRI          |              | X-Ray        |              | Ultrasound   |              | Fundus       |              | Endoscopy    |              | Avg          |              |
|------------------------------------|--------------|--------------|--------------|--------------|--------------|--------------|--------------|--------------|--------------|--------------|--------------|--------------|--------------|--------------|
|                                    | Dice         | IoU          |
| <i>SAM based methods</i>           |              |              |              |              |              |              |              |              |              |              |              |              |              |              |
| SAM2-Point (Ravi et al., 2024)     | 0.610        | 0.531        | 0.488        | 0.412        | 0.546        | 0.422        | 0.528        | 0.408        | 0.362        | 0.265        | 0.659        | 0.597        | 0.532        | 0.439        |
| SAM2-Box (Ravi et al., 2024)       | 0.837        | 0.754        | 0.838        | 0.748        | 0.827        | 0.733        | 0.871        | 0.779        | 0.717        | 0.574        | 0.922        | 0.872        | 0.835        | 0.743        |
| MedSAM-Point (Ma et al., 2025b)    | 0.747        | 0.640        | 0.667        | 0.584        | 0.843        | 0.776        | 0.591        | 0.467        | 0.414        | 0.346        | 0.822        | 0.736        | 0.681        | 0.592        |
| MedSAM-Box (Ma et al., 2025b)      | 0.847        | 0.759        | 0.854        | 0.768        | 0.897        | 0.836        | 0.890        | 0.806        | 0.846        | 0.743        | 0.925        | 0.872        | 0.876        | 0.797        |
| IMISNet-Point (Cheng et al., 2025) | 0.674        | 0.580        | 0.678        | 0.556        | 0.578        | 0.449        | 0.489        | 0.371        | 0.677        | 0.528        | 0.781        | 0.681        | 0.646        | 0.527        |
| IMISNet-Box (Cheng et al., 2025)   | 0.805        | 0.727        | 0.849        | 0.758        | 0.706        | 0.628        | 0.569        | 0.483        | 0.841        | 0.733        | 0.905        | 0.846        | 0.779        | 0.696        |
| <i>MLLM based methods</i>          |              |              |              |              |              |              |              |              |              |              |              |              |              |              |
| LISA (Lai et al., 2024)            | 0.088        | 0.051        | 0.110        | 0.063        | 0.322        | 0.230        | 0.385        | 0.280        | 0.036        | 0.019        | 0.282        | 0.222        | 0.204        | 0.144        |
| GLAMM (Rasheed et al., 2024)       | 0.088        | 0.053        | 0.106        | 0.061        | 0.285        | 0.194        | 0.402        | 0.294        | 0.027        | 0.014        | 0.245        | 0.179        | 0.192        | 0.132        |
| HyperSeg (Wei et al., 2024a)       | 0.098        | 0.069        | 0.153        | 0.101        | 0.336        | 0.231        | 0.434        | 0.336        | 0.023        | 0.012        | 0.396        | 0.342        | 0.240        | 0.182        |
| Seg-R1 (You & Wu, 2025)            | 0.099        | 0.064        | 0.126        | 0.075        | 0.417        | 0.318        | 0.490        | 0.382        | 0.455        | 0.325        | 0.533        | 0.471        | 0.353        | 0.272        |
| MedPLIB (Huang et al., 2025b)      | 0.052        | 0.038        | 0.177        | 0.136        | 0.115        | 0.075        | 0.088        | 0.056        | 0.298        | 0.201        | 0.132        | 0.097        | 0.144        | 0.101        |
| UniBiomed (Wu et al., 2025b)       | <u>0.724</u> | <u>0.634</u> | <b>0.807</b> | <b>0.716</b> | <u>0.817</u> | <u>0.748</u> | <u>0.736</u> | <u>0.618</u> | 0.794        | 0.668        | 0.778        | 0.704        | <u>0.776</u> | <b>0.681</b> |
| Citrus-V(Wang et al., 2025a)       | 0.363        | 0.302        | 0.326        | 0.258        | 0.624        | 0.536        | 0.134        | 0.094        | 0.782        | 0.655        | 0.666        | 0.616        | 0.482        | 0.410        |
| Qwen3-VL+MedSAM2 (RL only)         | 0.401        | 0.346        | 0.647        | 0.559        | <b>0.834</b> | <b>0.779</b> | 0.718        | 0.600        | 0.775        | 0.644        | 0.695        | 0.631        | 0.678        | 0.593        |
| Ours-IMISNet                       | <b>0.732</b> | <b>0.654</b> | 0.783        | 0.685        | 0.798        | 0.723        | 0.658        | 0.547        | <u>0.803</u> | <u>0.678</u> | 0.803        | <u>0.736</u> | 0.763        | 0.670        |
| Ours-MedSAM2                       | 0.720        | 0.633        | <u>0.793</u> | <u>0.701</u> | 0.833        | <u>0.775</u> | <b>0.793</b> | <b>0.685</b> | <b>0.813</b> | <b>0.692</b> | <b>0.811</b> | <b>0.744</b> | <b>0.794</b> | <b>0.705</b> |

By leveraging this relative advantage formulation, we ensure that the model learns to prioritize higher-reward trajectories. Through carefully designed RL training, the agent becomes capable of interpreting complex target descriptions and performing pixel-level reasoning via iterative tool invocations. Moreover, we specifically curate 9K high-quality samples for the RL training data to effectively guide this learning process and ensure strong policy convergence during the RL rollout. This selection focuses on challenging instances that necessitated 3–5 interaction rounds under both Box-to-Point and Sequential-Click paradigms, thereby exposing the model to complex decision-making scenarios and maximizing the efficiency of the optimization strategy.

## 4. Experiments

### 4.1. Experiments Setting

**Datasets.** We utilize a comprehensive collection of 21 open-source datasets spanning 6 modalities, including CT (Landman et al., 2015; Ji et al., 2022; Ma et al., 2022; Heller et al., 2023; Armato III et al., 2011), MRI (Bernard et al., 2018; Ji et al., 2022; Buda et al., 2019), X-Ray (Jaeger et al., 2014; Chowdhury et al., 2020; Khaled et al., 2021), Ultrasound (Vitale et al., 2020; Jieyun & ZhanHong, 2024), Fundus (Orlando et al., 2020), and Endoscopy (Ngoc Lan et al., 2021; Ali et al., 2023). All data formats are standardized following previous methods (Zhao et al., 2025; Wu et al.,

2025b). Details are available in the Appendix.

**Implementation Details.** In our experiments, the policy model is based on the Qwen3-VL-8B (Bai et al., 2025), and the interactive segmentation models used in our work include general-purpose model SAM2.1-Base (Ravi et al., 2024), and medical domain-specific models MedSAM2 (Ma et al., 2025b) and IMISNet (Cheng et al., 2025). The SFT stage is implemented using Llama-Factory (Zheng et al., 2024b) with a learning rate of 1e-5 and the batch size is 64. The RL stage is implemented by the Verl framework (Sheng et al., 2024) with a learning rate of 1e-5, batch size of 8 and sampling number of 8, the maximum interaction turn is 5. All experiments are conducted on 8× NVIDIA H20 GPUs.

### 4.2. Comparison Experiment

**Baselines and Protocols.** In this section, we conduct a comprehensive evaluation of our MedSAM-Agent against existing state-of-the-art (SOTA) methods, including the interactive segmentations like general-purpose model SAM2 (Ravi et al., 2024) and domain-specific models such as MedSAM2 (Ma et al., 2025b) and IMISNet (Cheng et al., 2025). For these baselines, we report results using both *Point* and *Box* prompts. “Point” results are generated using the center of the ground-truth mask, while “Box” results utilize corresponding bounding boxes. The *Box* prompt performance is generally regarded as the empirical upper bound for single-turn interactive segmentation. Furthermore, we

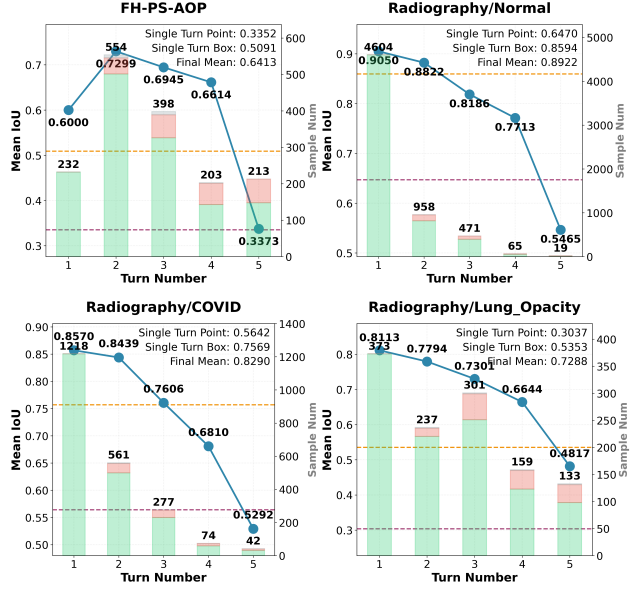


**Figure 3. Analysis of multi-turn interaction.** The orange and purple lines represent the performance of the static Single-Turn Box and Single-Turn Point prompts, respectively, where inputs are derived from ground-truth bounding boxes and centroids. The blue line plots the Mean IoU across successive interaction turns. The bar charts illustrate the distribution of sample outcomes at each turn, where green, red, and grey segments denote the proportion of samples exhibiting improved, declined, or unchanged IoU. The segmentation tool is IMISNet (Cheng et al., 2025).

benchmark against SOTA MLLM-based methods, including four general-domain models (LISA (Lai et al., 2024), GLAMM (Rasheed et al., 2024), HyperSeg (Wei et al., 2024a), and Seg-R1 (You & Wu, 2025)) and three specialized medical MLLMs (MedPLIB (Huang et al., 2025b), UniBioMed (Wu et al., 2025b), and Citrus-V (Wang et al., 2025a)).

**Segmentation Performance.** Table 1 shows the quantitative comparison across 6 medical imaging modalities. We observe that general-purpose MLLMs, such as LISA (Lai et al., 2024), exhibit poor performance on these medical datasets. This suggests that the `<seg>` token-based paradigm suffers from limited generalization and faces significant hurdles when transferring to the specialized medical domain without extensive in-domain fine-tuning. In contrast, although Seg-R1 (You & Wu, 2025) was not specifically fine-tuned on medical domain data, it significantly outperforms other general-purpose MLLMs. This suggests that RL-based optimization inherently equips models with superior structural reasoning and out-of-distribution generalization for segmentation tasks, even when navigating unfamiliar medical modalities. Furthermore, specialized medical models such as UniBioMed and Citrus-V show marked improvements over general-purpose baselines, underscoring the vital importance of domain-specific medical knowledge. Build-

**Table 2. Performance comparison of various policy models and segmentation frameworks.** (Tr/Te denotes the segmentation models used during training and testing, respectively; ‘-’ indicates zero-shot evaluation.

| Policy Model  | Seg Model (Tr/Te) | BTCV         |              | PolypGen     |              |
|---------------|-------------------|--------------|--------------|--------------|--------------|
|               |                   | Dice         | IoU          | Dice         | IoU          |
| GPT-4o        | - / MedSAM2       | 0.122        | 0.104        | 0.549        | 0.481        |
| Qwen2.5-VL-7B | - / MedSAM2       | 0.117        | 0.098        | 0.389        | 0.331        |
| Qwen3-VL-8B   | - / MedSAM2       | 0.130        | 0.113        | 0.669        | 0.605        |
| Qwen3-VL-8B   | - / IMIS          | 0.101        | 0.080        | 0.539        | 0.466        |
| Qwen3-VL-8B   | IMIS / IMIS       | <b>0.780</b> | <b>0.702</b> | 0.793        | 0.719        |
| Qwen3-VL-8B   | MedSAM2 / MedSAM2 | 0.773        | 0.690        | <b>0.809</b> | 0.735        |
| Qwen3-VL-8B   | IMIS / SAM2       | 0.764        | 0.680        | 0.805        | 0.740        |
| Qwen3-VL-8B   | IMIS / MedSAM2    | 0.769        | 0.687        | 0.799        | 0.726        |
| Qwen3-VL-8B   | MedSAM2 / IMIS    | 0.761        | 0.682        | 0.798        | 0.720        |
| Qwen3-VL-8B   | MedSAM2 / SAM2    | 0.763        | 0.677        | 0.808        | <b>0.739</b> |

ing upon this, MedSAM-Agent further extends these gains by internalizing multi-turn interaction logic, consistently achieving high mask fidelity across all evaluated datasets. Details of the segmentation performance of 21 datasets are shown in the Appendix.

Moreover, we analyze the transformative power of the multi-turn strategic interaction of MedSAM-Agent. To demonstrate the efficacy of autonomous interaction, we compare our agent against static baseline paradigms, specifically Single-Turn Point and Single-Turn Box prompts where inputs are directly derived from ground-truth centroids and bounding boxes. As illustrated in Fig. 3, which details the performance trajectories on the FH-PS-AOP (Jieyun & ZhanHong, 2024) and Radiography (Chowdhury et al., 2020) datasets, MedSAM-Agent outperforms these ideal single-turn baselines. Notably, the Final Mean IoU achieved by our agent exceeds the theoretical upper bound of static prompts across all evaluated modalities, proving that the agent has internalized a sophisticated refinement logic rather than simple tool invocation. The stacked bar charts further quantify this effectiveness: the predominance of green segments signifies that the vast majority of autonomous interactions result in substantial IoU gains. Furthermore, the diminishing sample counts across successive turns confirm the agent’s ability to adaptively select the optimal interaction depth, effectively balancing segmentation precision with procedural efficiency.

**Zero-shot Tool Agnosticism.** To investigate the model’s ability to generalize across various interactive segmentation backends, we conducted a cross-tool evaluation by separately synthesizing training trajectories using two distinct models, MedSAM2 and IMISNet, and subsequently testing the learned policies against alternative engines including SAM2. Our experiments reveal that while trajectories curated via MedSAM2 generally result in superior

agent performance due to its higher fidelity in mask boundary delineations, the resulting agent exhibits exceptional zero-shot generalization regardless of the training backend. As summarized in Table 2, an agent trained on one specific tool can be seamlessly interfaced with alternative backends at inference time with negligible performance degradation. This tool-agnostic capability suggests that the RL-based policy has successfully decoupled high-level strategic decision-making involving optimal point placement and autonomous stopping criteria from the low-level mask generation mechanics of specific tools. Consequently, MedSAM-Agent successfully internalizes a universal interaction logic, demonstrating its robust transferability and potential for integration into diverse clinical workflows independent of the underlying segmentation engine.

### 4.3. Ablation Study

**Effectiveness of Action Strategies.** We first investigate the impact of different interaction strategies on segmentation performance. As illustrated in Table 3, the Hybrid strategy clearly outperforms any single-strategy approach. Compared to a purely Sequential-Click strategy, the use of the box-to-point strategy alone significantly improves the IoU from 0.623 to 0.649 while reducing the average interaction turns from 2.94 to 2.06. This demonstrates that the box strategy provides a superior spatial constraint that effectively defines target boundaries with fewer interactions. Most importantly, the Hybrid strategy achieves the highest performance among the SFT variants, reaching an IoU of 0.686. This success stems from the fact that the hybrid approach aligns with human intuition: it leverages the box to establish a reliable global context and uses subsequent points for precise local refinement. These results prove that combining box and point strategies is the most effective way to navigate complex medical lesions, as it minimizes redundant actions while maximizing segmentation fidelity.

**Analysis of Training Strategies.** We evaluate three training paradigms: direct RL from scratch, SFT only, and our combined SFT+RL approach (Table 3). Direct RL exhibits a clear performance dichotomy across different modalities. In scenarios with prominent lesions and relatively simple backgrounds, such as X-ray and Endoscopy, direct RL can achieve competitive results as the agent easily identifies the target regions. However, it fails to achieve precise localization in more challenging modalities like CT and MRI, where the vast search space and low tissue contrast pose significant obstacles (Table 1). This discrepancy highlights that while RL is adept at strategy optimization, it struggles with the initial grounding problem in complex medical contexts. In contrast, our SFT cold-start phase establishes essential anatomical grounding and domain knowledge. The subsequent RL stage then enables the model to generalize across tools and optimize for procedural efficiency. This two-stage

**Table 3. Ablation study.** Metrics are average Dice and IoU, and the segmentation tool is MedSAM2 (Ma et al., 2025b).

| Setting                        | Dice         | IoU          | $n_{turn}$  |
|--------------------------------|--------------|--------------|-------------|
| Qwen3-VL-8B base               | 0.263        | 0.178        | 4.34        |
| + Cold-start SFT only (Hybrid) | 0.769        | 0.686        | 2.35        |
| - only Sequential-Click        | 0.719        | 0.623        | 2.94        |
| - only Box-to-Point            | 0.745        | 0.649        | <b>2.06</b> |
| + RL only                      | 0.678        | 0.593        | 2.23        |
| + Cold-start SFT + RL (Full)   | <b>0.794</b> | <b>0.705</b> | 2.11        |
| - w/o $R_{imp}$                | 0.772        | 0.688        | 2.08        |
| - w/o $R_{over}$               | 0.785        | 0.693        | 2.24        |
| - w/o $R_{cost}$               | 0.788        | 0.696        | 2.26        |

pipeline ensures the agent possesses both the anatomical awareness required for medical precision and the strategic flexibility for efficient, multi-step interaction.

**Impact of Reward Design.** To evaluate the contribution of each component in our proposed reward framework, we conduct an ablation study on the process-aware rewards as shown in Table 3. Our results indicate that while the baseline model achieves basic segmentation, it often suffers from inefficient interaction trajectories and redundant operations. The inclusion of the  $R_{imp}$  is critical for maintaining mask fidelity throughout the interaction; its removal results in a decline in Dice score from 0.794 to 0.772 and a drop in IoU to 0.688. The  $R_{over}$  serves as a vital regularizer for the agent to determine the optimal timing for task completion. When  $R_{over}$  is excluded, the agent fails to terminate the process at optimal states, leading to an increase in average interaction turns ( $n_{turn}$ ) from 2.11 to 2.24. Similarly, the absence of the  $R_{cost}$  confirms that our process-level supervision effectively discourages redundant strategies. Overall, the two-stage pipeline achieves the superior balance of precision and interaction turns, demonstrating that process-aware rewards successfully align the agent’s behavior with both clinical accuracy and operational efficiency.

## 5. Conclusion

In this paper, we propose MedSAM-Agent, a novel framework that shifts the medical image segmentation paradigm from static classification to an autonomous, multi-step decision-making process. By addressing the limitations of current interactive models that depend on human guidance and automated MLLM approaches that lack iterative refinement, our method successfully bridges the gap between high-level reasoning and precise tool interaction. Through a hybrid prompting strategy and a two-stage training pipeline optimized by fine-grained process rewards, we enable the model to function as a self-refinement agent capable of achieving expert-level segmentation across diverse

imaging modalities. Experimental results underscore the framework’s superior performance and robust generalization, demonstrating its potential to reduce the workload of clinical professionals.

## References

Ali, S., Jha, D., Ghatwary, N., Realdon, S., Cannizzaro, R., Salem, O. E., Lamarque, D., Daul, C., Riegler, M. A., Anonsen, K. V., et al. A multi-centre polyp detection and segmentation dataset for generalisability assessment. *Scientific Data*, 10(1):75, 2023.

Armato III, S. G., McLennan, G., Bidaut, L., McNitt-Gray, M. F., Meyer, C. R., Reeves, A. P., Zhao, B., Aberle, D. R., Henschke, C. I., Hoffman, E. A., et al. The lung image database consortium (lidc) and image database resource initiative (idri): a completed reference database of lung nodules on ct scans. *Medical physics*, 38(2):915–931, 2011.

Bai, S., Chen, K., Liu, X., Wang, J., Ge, W., Song, S., Dang, K., Wang, P., Wang, S., Tang, J., Zhong, H., Zhu, Y., Yang, M., Li, Z., Wan, J., Wang, P., Ding, W., Fu, Z., Xu, Y., Ye, J., Zhang, X., Xie, T., Cheng, Z., Zhang, H., Yang, Z., Xu, H., and Lin, J. Qwen2.5-vl technical report. *arXiv preprint arXiv:2502.13923*, 2025.

Bernard, O., Lalande, A., Zotti, C., Cervenansky, F., Yang, X., Heng, P.-A., Cetin, I., Lekadir, K., Camara, O., Ballester, M. A. G., et al. Deep learning techniques for automatic mri cardiac multi-structures segmentation and diagnosis: is the problem solved? *IEEE Transactions on Medical Imaging*, 37(11):2514–2525, 2018.

Buda, M., Saha, A., and Mazurowski, M. A. Association of genomic subtypes of lower-grade gliomas with shape features automatically extracted by a deep learning algorithm. *Computers in Biology and Medicine*, 109:218–225, 2019.

Butoi, V. I., Ortiz, J. J. G., Ma, T., Sabuncu, M. R., Guttag, J., and Dalca, A. V. Universeg: Universal medical image segmentation. In *ICCV*, pp. 21438–21451, 2023.

Chen, J., Lu, Y., Yu, Q., Luo, X., Adeli, E., Wang, Y., Lu, L., Yuille, A. L., and Zhou, Y. Transunet: Transformers make strong encoders for medical image segmentation. *arXiv preprint arXiv:2102.04306*, 2021.

Chen, J., Gui, C., Ouyang, R., Gao, A., Chen, S., Chen, G. H., Wang, X., Zhang, R., Cai, Z., Ji, K., Yu, G., Wan, X., and Wang, B. Huatuogpt-vision, towards injecting medical visual knowledge into multimodal llms at scale, 2024a.

Chen, K., Rui, S., Jiang, Y., Wu, J., Zheng, Q., Song, C., Wang, X., Zhou, M., and Liu, M. Think twice to see more: Iterative visual reasoning in medical vlms. *arXiv preprint arXiv:2510.10052*, 2025.

Chen, W., Shen, L., Lin, J., Luo, J., Li, X., and Yuan, Y. Fine-grained image-text alignment in medical imaging enables explainable cyclic image-report generation. In *Proceedings of the 62nd Annual Meeting of the Association for Computational Linguistics (Volume 1: Long Papers)*, pp. 9494–9509, 2024b.

Cheng, J., Fu, B., Ye, J., Wang, G., Li, T., Wang, H., Li, R., Yao, H., Cheng, J., Li, J., et al. Interactive medical image segmentation: A benchmark dataset and baseline. In *Proceedings of the Computer Vision and Pattern Recognition Conference*, pp. 20841–20851, 2025.

Chowdhury, M. E., Rahman, T., Khandakar, A., Mazhar, R., Kadir, M. A., Mahbub, Z. B., Islam, K. R., Khan, M. S., Iqbal, A., Al Emadi, N., et al. Can ai help in screening viral and covid-19 pneumonia? *IEEE Access*, 8:132665–132676, 2020.

Fan, D.-P., Ji, G.-P., Zhou, T., Chen, G., Fu, H., Shen, J., and Shao, L. Pranet: Parallel reverse attention network for polyp segmentation, 2020. URL <https://arxiv.org/abs/2006.11392>.

Fathi, N., Kumar, A., and Arbel, T. Aura: A multi-modal medical agent for understanding, reasoning and annotation. In *International Workshop on Agentic AI for Medicine*, pp. 105–114. Springer, 2025.

Feng, K., Gong, K., Li, B., Guo, Z., Wang, Y., Peng, T., Wu, J., Zhang, X., Wang, B., and Yue, X. Video-r1: Reinforcing video reasoning in mllms. *arXiv preprint arXiv:2503.21776*, 2025.

Gong, S., Zhong, Y., Ma, W., Li, J., Wang, Z., Zhang, J., Heng, P.-A., and Dou, Q. 3dsam-adapter: Holistic adaptation of sam from 2d to 3d for promptable tumor segmentation. *Medical Image Analysis*, 98:103324, 2024.

He, X., Zhang, Y., Mou, L., Xing, E., and Xie, P. Pathvqa: 30000+ questions for medical visual question answering. *arXiv preprint arXiv:2003.10286*, 2020.

Heller, N., Isensee, F., Trofimova, D., Tejpaul, R., Zhao, Z., Chen, H., Wang, L., Golts, A., Khapun, D., Shats, D., et al. The kits21 challenge: Automatic segmentation of kidneys, renal tumors, and renal cysts in corticomedullary-phase ct. *arXiv preprint arXiv:2307.01984*, 2023.

Hu, Y., Li, T., Lu, Q., Shao, W., He, J., Qiao, Y., and Luo, P. Omnimedvqa: A new large-scale comprehensive evaluation benchmark for medical lilm. In *Proceedings of the IEEE/CVF Conference on Computer Vision and Pattern Recognition*, pp. 22170–22183, 2024.

Huang, J., Xu, Z., Zhou, J., Liu, T., Xiao, Y., Ou, M., Ji, B., Li, X., and Yuan, K. Sam-r1: Leveraging sam for reward feedback in multimodal segmentation via reinforcement learning. *arXiv preprint arXiv:2505.22596*, 2025a.

Huang, X., Shen, L., Liu, J., Shang, F., Li, H., Huang, H., and Yang, Y. Towards a multimodal large language model with pixel-level insight for biomedicine. In *Proceedings of the AAAI Conference on Artificial Intelligence*, volume 39, pp. 3779–3787, 2025b.

Huang, Y., Peng, Z., Zhao, Y., Yang, P., Yang, X., and Shen, W. Medseg-r: Reasoning segmentation in medical images with multimodal large language models. *arXiv preprint arXiv:2506.10465*, 2025c.

Isensee, F., Jaeger, P. F., Kohl, S. A., Petersen, J., and Maier-Hein, K. H. nnu-net: a self-configuring method for deep learning-based biomedical image segmentation. *Nature methods*, 18(2):203–211, 2021.

Jaeger, S., Candemir, S., Antani, S., Wang, Y.-X. J., Lu, P.-X., and Thoma, G. Two public chest x-ray datasets for computer-aided screening of pulmonary diseases. *Quantitative imaging in medicine and surgery*, 4(6):475, 2014.

Ji, Y., Bai, H., Ge, C., Yang, J., Zhu, Y., Zhang, R., Li, Z., Zhang, L., Ma, W., Wan, X., et al. Amos: A large-scale abdominal multi-organ benchmark for versatile medical image segmentation. *Advances in Neural Information Processing Systems*, 35:36722–36732, 2022.

Jiang, S., Wang, Y., Song, S., Hu, T., Zhou, C., Pu, B., Zhang, Y., Yang, Z., Feng, Y., Zhou, J. T., et al. Hulumed: A transparent generalist model towards holistic medical vision-language understanding. *arXiv preprint arXiv:2510.08668*, 2025a.

Jiang, Y., Zhang, Y., Zhang, P., Li, Y., Chen, J., Shi, X., and Zhen, S. Incentivizing tool-augmented thinking with images for medical image analysis. *arXiv preprint arXiv:2512.14157*, 2025b.

Jiang, Y., Li, Q., Xu, B., Sun, H., Ding, C., Dong, J., Cai, Y., Zhang, X., and Yin, J. Ibisagent: Reinforcing pixel-level visual reasoning in mllms for universal biomedical object referring and segmentation. *arXiv preprint arXiv:2601.03054*, 2026.

Jieyun, B. and ZhanHong, O. Pubic symphysis-fetal head segmentation and angle of progression, 2024.

Khaled, R. et al. Categorized digital database for low energy and subtracted contrast enhanced spectral mammography images. *The Cancer Imaging Archive*, 2021.

Kirillov, A., Mintun, E., Ravi, N., Mao, H., Rolland, C., Gustafson, L., Xiao, T., Whitehead, S., Berg, A. C., Lo, W.-Y., et al. Segment anything. In *CVPR*, pp. 4015–4026, 2023.

Konwer, A., Yang, Z., Bas, E., Xiao, C., Prasanna, P., Bhatia, P., and Kass-Hout, T. Enhancing sam with efficient prompting and preference optimization for semi-supervised medical image segmentation. In *CVPR*, pp. 20990–21000, 2025.

Lai, X., Tian, Z., Chen, Y., Li, Y., Yuan, Y., Liu, S., and Jia, J. Lisa: Reasoning segmentation via large language model. In *CVPR*, pp. 9579–9589, 2024.

Lai, X., Li, J., Li, W., Liu, T., Li, T., and Zhao, H. Mini-o3: Scaling up reasoning patterns and interaction turns for visual search. *arXiv preprint arXiv:2509.07969*, 2025a.

Lai, Y., Zhong, J., Li, M., Zhao, S., and Yang, X. Med-r1: Reinforcement learning for generalizable medical reasoning in vision-language models. *arXiv preprint arXiv:2503.13939*, 2025b.

Landman, B., Xu, Z., Iglesias, J., Styner, M., Langerak, T., and Klein, A. Miccai multi-atlas labeling beyond the cranial vault—workshop and challenge. In *Proc. MICCAI Multi-Atlas Labeling Beyond Cranial Vault—Workshop Challenge*, volume 5, pp. 12, 2015.

Lau, J. J., Gayen, S., Ben Abacha, A., and Demner-Fushman, D. A dataset of clinically generated visual questions and answers about radiology images. *Scientific data*, 5(1):1–10, 2018.

Li, B., Yan, T., Pan, Y., Luo, J., Ji, R., Ding, J., Xu, Z., Liu, S., Dong, H., Lin, Z., et al. Mmedagent: Learning to use medical tools with multi-modal agent. *arXiv preprint arXiv:2407.02483*, 2024.

Li, C., Liu, X., Li, W., Wang, C., Liu, H., Liu, Y., Chen, Z., and Yuan, Y. U-kan makes strong backbone for medical image segmentation and generation. In *Proceedings of the AAAI Conference on Artificial Intelligence*, volume 39, pp. 4652–4660, 2025a.

Li, C.-Y., Chang, K.-J., Yang, C.-F., Wu, H.-Y., Chen, W., Bansal, H., Chen, L., Yang, Y.-P., Chen, Y.-C., Chen, S.-P., et al. Towards a holistic framework for multimodal llm in 3d brain ct radiology report generation. *Nature Communications*, 16(1):2258, 2025b.

Liu, B., Zhan, L.-M., Xu, L., Ma, L., Yang, Y., and Wu, X.-M. Slake: A semantically-labeled knowledge-enhanced dataset for medical visual question answering. In *2021 IEEE 18th international symposium on biomedical imaging (ISBI)*, pp. 1650–1654. IEEE, 2021.

Liu, S., Zheng, B., Chen, W., Peng, Z., Yin, Z., Shao, J., Hu, J., and Yuan, Y. Endobench: A comprehensive evaluation of multi-modal large language models for endoscopy analysis, 2025a.

Liu, Y., Peng, B., Zhong, Z., Yue, Z., Lu, F., Yu, B., and Jia, J. Seg-zero: Reasoning-chain guided segmentation via cognitive reinforcement. *arXiv preprint arXiv:2503.06520*, 2025b.

Liu, Y., Qu, T., Zhong, Z., Peng, B., Liu, S., Yu, B., and Jia, J. Visionreasoner: Unified visual perception and reasoning via reinforcement learning. *arXiv preprint arXiv:2505.12081*, 2025c.

Liu, Z., Sun, Z., Zang, Y., Dong, X., Cao, Y., Duan, H., Lin, D., and Wang, J. Visual-rft: Visual reinforcement fine-tuning. *ICCV*, 2025d.

Luo, X., Liao, W., Xiao, J., Chen, J., Song, T., Zhang, X., Li, K., Metaxas, D. N., Wang, G., and Zhang, S. Word: A large scale dataset, benchmark and clinical applicable study for abdominal organ segmentation from ct image. *Medical Image Analysis*, 82:102642, 2022.

Ma, J., Zhang, Y., Gu, S., An, X., Wang, Z., Ge, C., Wang, C., Zhang, F., Wang, Y., Xu, Y., et al. Fast and low-gpu-memory abdomen ct organ segmentation: the flare challenge. *Medical Image Analysis*, 82:102616, 2022.

Ma, J., He, Y., Li, F., Han, L., You, C., and Wang, B. Segment anything in medical images. *Nature Communications*, 15(1):654, 2024.

Ma, J., Xu, Y., Zhou, F., Wang, Y., Jin, C., Guo, Z., Wu, J., Tang, O. K., Zhou, H., Wang, X., et al. Pathbench: A comprehensive comparison benchmark for pathology foundation models towards precision oncology. *arXiv preprint arXiv:2505.20202*, 2025a.

Ma, J., Yang, Z., Kim, S., Chen, B., Baharoon, M., Fallahpour, A., Asakereh, R., Lyu, H., and Wang, B. Medsam2: Segment anything in 3d medical images and videos. *arXiv preprint arXiv:2504.03600*, 2025b.

Nath, V., Li, W., Yang, D., Myronenko, A., Zheng, M., Lu, Y., Liu, Z., Yin, H., Law, Y. M., Tang, Y., et al. Vila-m3: Enhancing vision-language models with medical expert knowledge. In *Proceedings of the Computer Vision and Pattern Recognition Conference*, pp. 14788–14798, 2025.

Ngoc Lan, P., An, N. S., Hang, D. V., Long, D. V., Trung, T. Q., Thuy, N. T., and Sang, D. V. Neounet: Towards accurate colon polyp segmentation and neoplasm detection. In *Advances in visual computing: 16th international symposium, ISVC 2021, virtual event, October 4-6, 2021, proceedings, part II*, pp. 15–28. Springer, 2021.

Ning, J., Li, W., Tang, C., Lin, J., Ma, C., Zhang, C., Liu, J., Chen, Y., Gao, S., Liu, L., et al. Unimedvl: Unifying medical multimodal understanding and generation through observation-knowledge-analysis. *arXiv preprint arXiv:2510.15710*, 2025.

OpenAI. Thinking with images, 2025. URL <https://openai.com/index/thinking-with-images/>.

Orlando, J. I., Fu, H., Breda, J. B., Van Keer, K., Bathula, D. R., Diaz-Pinto, A., Fang, R., Heng, P.-A., Kim, J., Lee, J., et al. Refuge challenge: A unified framework for evaluating automated methods for glaucoma assessment from fundus photographs. *Medical Image Analysis*, 59: 101570, 2020.

Pan, J., Liu, C., Wu, J., Liu, F., Zhu, J., Li, H. B., Chen, C., Ouyang, C., and Rueckert, D. Medvlm-r1: Incentivizing medical reasoning capability of vision-language models (vlms) via reinforcement learning. In *MICCAI*, pp. 337–347. Springer, 2025.

Peng, Y., Zhang, G., Zhang, M., You, Z., Liu, J., Zhu, Q., Yang, K., Xu, X., Geng, X., and Yang, X. Lmm-r1: Empowering 3b lmms with strong reasoning abilities through two-stage rule-based rl. *arXiv preprint arXiv:2503.07536*, 2025.

Rasheed, H., Maaz, M., Shaji, S., Shaker, A., Khan, S., Cholakkal, H., Anwer, R. M., Xing, E., Yang, M.-H., and Khan, F. S. Glamm: Pixel grounding large multimodal model. In *CVPR*, pp. 13009–13018, 2024.

Ravi, N., Gabeur, V., Hu, Y.-T., Hu, R., Ryali, C., Ma, T., Khedr, H., Rädle, R., Rolland, C., Gustafson, L., et al. Sam 2: Segment anything in images and videos. *arXiv preprint arXiv:2408.00714*, 2024.

Ronneberger, O., Fischer, P., and Brox, T. U-net: Convolutional networks for biomedical image segmentation. In *MICCAI*, pp. 234–241. Springer, 2015.

Ru, J., Yan, S., Yin, Y., Zou, Y., and Ge, Z. Dermogpt: Open weights and open data for morphology-grounded dermatological reasoning mlms. *arXiv preprint arXiv:2601.01868*, 2026.

Schulman, J., Wolski, F., Dhariwal, P., Radford, A., and Klimov, O. Proximal policy optimization algorithms, 2017. URL <https://arxiv.org/abs/1707.06347>.

Sellergren, A., Kazemzadeh, S., Jaroensri, T., Kiraly, A., Traverse, M., Kohlberger, T., Xu, S., Jamil, F., Hughes, C., Lau, C., et al. Medgemma technical report. *arXiv preprint arXiv:2507.05201*, 2025.

Shao, Z., Wang, P., Zhu, Q., Xu, R., Song, J., Bi, X., Zhang, H., Zhang, M., Li, Y., et al. Deepseekmath: Pushing the limits of mathematical reasoning in open language models. *arXiv preprint arXiv:2402.03300*, 2024.

Shen, H., Liu, P., Li, J., Fang, C., Ma, Y., Liao, J., Shen, Q., Zhang, Z., Zhao, K., Zhang, Q., et al. Vlm-r1: A stable and generalizable r1-style large vision-language model. *arXiv preprint arXiv:2504.07615*, 2025a.

Shen, H., Zhao, K., Zhao, T., Xu, R., Zhang, Z., Zhu, M., and Yin, J. Zoomeye: Enhancing multimodal llms with human-like zooming capabilities through tree-based image exploration. In *EMNLP*, pp. 6613–6629, 2025b.

Sheng, G., Zhang, C., Ye, Z., Wu, X., Zhang, W., Zhang, R., Peng, Y., Lin, H., and Wu, C. Hybridflow: A flexible and efficient rlhf framework. *arXiv preprint arXiv:2409.19256*, 2024.

Su, A., Wang, H., Ren, W., Lin, F., and Chen, W. Pixel reasoner: Incentivizing pixel-space reasoning with curiosity-driven reinforcement learning. *arXiv preprint arXiv:2505.15966*, 2025a.

Su, Z., Li, L., Song, M., Hao, Y., Yang, Z., Zhang, J., Chen, G., Gu, J., Li, J., Qu, X., et al. Openthinkimg: Learning to think with images via visual tool reinforcement learning. *arXiv preprint arXiv:2505.08617*, 2025b.

Vitale, S., Orlando, J. I., Iarussi, E., and Larrabide, I. Improving realism in patient-specific abdominal ultrasound simulation using cyclegans. *International Journal of Computer Assisted Radiology and Surgery*, 15(2):183–192, 2020.

Wang, G., Zhao, J., Liu, X., Liu, Y., Cao, X., Li, C., Liu, Z., Sun, Q., Zhou, F., Xing, H., et al. Citrus-v: Advancing medical foundation models with unified medical image grounding for clinical reasoning. *arXiv preprint arXiv:2509.19090*, 2025a.

Wang, H., Guo, S., Ye, J., Deng, Z., Cheng, J., Li, T., Chen, J., Su, Y., Huang, Z., Shen, Y., Fu, B., Zhang, S., He, J., and Qiao, Y. Sam-med3d: Towards general-purpose segmentation models for volumetric medical images, 2024. URL <https://arxiv.org/abs/2310.15161>.

Wang, L., Wang, H., Yang, H., Mao, J., Yang, Z., Shen, J., and Li, X. Interpretable bilingual multimodal large language model for diverse biomedical tasks. In *International Conference on Learning Representations*, 2025b.

Wang, W., Ma, Z., Ding, M., Zheng, S., Liu, S., Liu, J., Ji, J., Chen, W., Li, X., Shen, L., and Yuan, Y. Medical reasoning in the era of llms: A systematic review of enhancement techniques and applications, 2025c. URL <https://arxiv.org/abs/2508.00669>.

Wang, Z., Wu, J., Cai, L., Low, C. H., Yang, X., Li, Q., and Jin, Y. Medagent-pro: Towards evidence-based multimodal medical diagnosis via reasoning agentic workflow. *arXiv preprint arXiv:2503.18968*, 2025d.

Wei, C., Zhong, Y., Tan, H., Liu, Y., Zhao, Z., Hu, J., and Yang, Y. Hyperseg: Towards universal visual segmentation with large language model, 2024a. URL <https://arxiv.org/abs/2411.17606>.

Wei, X., Cao, J., Jin, Y., Lu, M., Wang, G., and Zhang, S. I-medsam: Implicit medical image segmentation with segment anything. In *ECCV*, pp. 90–107. Springer, 2024b.

Wu, J., Wang, Z., Hong, M., Ji, W., Fu, H., Xu, Y., Xu, M., and Jin, Y. Medical sam adapter: Adapting segment anything model for medical image segmentation. *Medical image analysis*, 102:103547, 2025a.

Wu, L., Nie, Y., He, S., Zhuang, J., Luo, L., Mahboobani, N., Vardhanabuti, V., Chan, R. C. K., Peng, Y., Rajpurkar, P., et al. Unibiomed: A universal foundation model for grounded biomedical image interpretation. *arXiv preprint arXiv:2504.21336*, 2025b.

Wu, M., Yang, J., Jiang, J., Li, M., Yan, K., Yu, H., Zhang, M., Zhai, C., and Nahrstedt, K. Vtool-r1: Vlms learn to think with images via reinforcement learning on multimodal tool use, 2025c. URL <https://arxiv.org/abs/2505.19255>.

Xu, H., Nie, Y., Wang, H., Chen, Y., Li, W., Ning, J., Liu, L., Wang, H., Zhu, L., Liu, J., et al. Medground-r1: Advancing medical image grounding via spatial-semantic rewarded group relative policy optimization. In *MICCAI*, pp. 391–401. Springer, 2025a.

Xu, W., Chan, H. P., Li, L., Aljunied, M., Yuan, R., Wang, J., Xiao, C., Chen, G., Liu, C., Li, Z., et al. Lingshu: A generalist foundation model for unified multimodal medical understanding and reasoning. *arXiv preprint arXiv:2506.07044*, 2025b.

Yan, Z., Diao, M., Yang, Y., Xu, J., Zhang, K., Jing, R., Yang, L., Liu, Y., Liang, K., and Ma, Z. Medreasoner: Reinforcement learning drives reasoning grounding from clinical thought to pixel-level precision. *arXiv preprint arXiv:2508.08177*, 2025.

Ye, J., Wang, G., Li, Y., Deng, Z., Li, W., Li, T., Duan, H., Huang, Z., Su, Y., Wang, B., et al. Gmai-mmbench: A comprehensive multimodal evaluation benchmark towards general medical ai. *Advances in Neural Information Processing Systems*, 37:94327–94427, 2024.

Ye, Y., Xie, Y., Zhang, J., Chen, Z., and Xia, Y. Uniseg: A prompt-driven universal segmentation model as well as a strong representation learner. In *MICCAI*, pp. 508–518. Springer, 2023.

You, Z. and Wu, Z. Seg-r1: Segmentation can be surprisingly simple with reinforcement learning. *arXiv preprint arXiv:2506.22624*, 2025.

Yu, Q., Zhang, Z., Zhu, R., Yuan, Y., Zuo, X., Yue, Y., Dai, W., Fan, T., Liu, G., Liu, L., et al. Dapo: An open-source llm reinforcement learning system at scale. *arXiv preprint arXiv:2503.14476*, 2025.

Zambrano Chaves, J. M., Huang, S.-C., Xu, Y., Xu, H., Usuyama, N., Zhang, S., Wang, F., Xie, Y., Khademi, M., Yang, Z., et al. A clinically accessible small multimodal radiology model and evaluation metric for chest x-ray findings. *Nature Communications*, 16(1):3108, 2025.

Zhang, H., Gu, X., Li, J., Ma, C., Bai, S., Zhang, C., Zhang, B., Zhou, Z., He, D., and Tang, Y. Thinking with videos: Multimodal tool-augmented reinforcement learning for long video reasoning. *arXiv preprint arXiv:2508.04416*, 2025a.

Zhang, J., Kim, J., O'Donoghue, B., and Boyd, S. Sample efficient reinforcement learning with reinforce, 2020. URL <https://arxiv.org/abs/2010.11364>.

Zhang, S., Liu, Q., Qin, G., Naumann, T., and Poon, H. Med-rlvr: Emerging medical reasoning from a 3b base model via reinforcement learning. *arXiv preprint arXiv:2502.19655*, 2025b.

Zhang, S., Zhang, Q., Zhang, S., Liu, X., Yue, J., Lu, M., Xu, H., Yao, J., Wei, X., Cao, J., et al. A generalist foundation model and database for open-world medical image segmentation. *Nature Biomedical Engineering*, pp. 1–16, 2025c.

Zhang, Y.-F., Lu, X., Yin, S., Fu, C., Chen, W., Hu, X., Wen, B., Jiang, K., Liu, C., Zhang, T., Fan, H., Chen, K., Chen, J., Ding, H., Tang, K., Zhang, Z., Wang, L., Yang, F., Gao, T., and Zhou, G. Thyme: Think beyond images, 2025d. URL <https://arxiv.org/abs/2508.11630>.

Zhao, T., Gu, Y., Yang, J., Usuyama, N., Lee, H. H., Kiblawi, S., Naumann, T., Gao, J., Crabtree, A., Abel, J., et al. A foundation model for joint segmentation, detection and recognition of biomedical objects across nine modalities. *Nature methods*, 22(1):166–176, 2025.

Zheng, C., Liu, S., Li, M., Chen, X.-H., Yu, B., Gao, C., Dang, K., Liu, Y., Men, R., Yang, A., Zhou, J., and Lin, J. Group sequence policy optimization, 2025a. URL <https://arxiv.org/abs/2507.18071>.

Zheng, L., Yin, L., Xie, Z., Sun, C. L., Huang, J., Yu, C. H., Cao, S., Kozyrakis, C., Stoica, I., Gonzalez, J. E., et al. Sqlang: Efficient execution of structured language model programs. *Advances in neural information processing systems*, 37:62557–62583, 2024a.

Zheng, Y., Zhang, R., Zhang, J., YeYanhan, Y., and Luo, Z. Llamafactory: Unified efficient fine-tuning of 100+ language models. In *ACL*, pp. 400–410, 2024b.

Zheng, Z., Yang, M., Hong, J., Zhao, C., Xu, G., Yang, L., Shen, C., and Yu, X. Deepeyes: Incentivizing “thinking with images” via reinforcement learning. *arXiv preprint arXiv:2505.14362*, 2025b.

Zhou, Z., Rahman Siddiquee, M. M., Tajbakhsh, N., and Liang, J. Unet++: A nested u-net architecture for medical image segmentation. In *International workshop on deep learning in medical image analysis*, pp. 3–11. Springer, 2018.

Zhu, M., Tian, Y., Chen, H., Zhou, C., Guo, Q., Liu, Y., Yang, M., and Shen, C. Segagent: Exploring pixel understanding capabilities in mllms by imitating human annotator trajectories. In *CVPR*, pp. 3686–3696, 2025.

# Supplementary

## A. Datasets

In our experiments, we utilize a comprehensive collection of 21 open-source datasets spanning 6 modalities, including CT (FLARE22 (Ma et al., 2022), KiTS (Heller et al., 2023), LIDC-IDRI (Armato III et al., 2011), BTCV (Landman et al., 2015), AMOS-CT (Ji et al., 2022), and WORD (Luo et al., 2022)), MRI (ACDC (Bernard et al., 2018), LGG (Buda et al., 2019), and AMOS-MRI (Ji et al., 2022)), X-Ray (CXRMask (Jaeger et al., 2014), Radiography series (Chowdhury et al., 2020), and CDD-CESM (Khaled et al., 2021)), Ultrasound (BreastUS (Vitale et al., 2020), LiverUS (Vitale et al., 2020), and FH-PS-AOP (Jieyun & ZhanHong, 2024)), Fundus (REFUGE (Orlando et al., 2020)), and Endoscopy (NeoPolyp (Ngoc Lan et al., 2021) and PolypGen (Ali et al., 2023)). All data formats are standardized following previous methods (Zhao et al., 2025; Wu et al., 2025b).

Table 4. Descriptions of datasets used in this work, including modalities, regions of interest, and the number of triplets (image-text-label).

| Dataset  | Modality     | Regions of interest   | Number  |
|--|--------------|-----------------------|---------|
| FLARE22 (Ma et al., 2022)                            | CT           | Abdomen organs        | 26,802  |
| KiTS (Heller et al., 2023)                           | CT           | Kidney & Kidney Tumor | 44,557  |
| LIDC-IDRI (Armato III et al., 2011)                  | CT           | Lung nodule           | 9,122   |
| BTCV (Landman et al., 2015)                          | CT           | Abdomen organs        | 12,176  |
| AMOS-CT (Ji et al., 2022)                            | CT           | Abdomen organs        | 138,371 |
| WORD (Luo et al., 2022)                              | CT           | Abdomen organs        | 58,898  |
| ACDC (Bernard et al., 2018)                          | MRI          | Heart                 | 7,666   |
| LGG (Buda et al., 2019)                              | MRI          | Brain Tumor           | 2,542   |
| AMOS-MRI (Ji et al., 2022)                           | MRI          | Abdomen               | 52,625  |
| CXRMask (Jaeger et al., 2014)                        | X-Ray        | Chest                 | 1,698   |
| Radiography-Lung-opacity (Chowdhury et al., 2020)    | X-Ray        | Chest                 | 6,012   |
| Radiography-Normal (Chowdhury et al., 2020)          | X-Ray        | Chest                 | 30,574  |
| Radiography-Viral-Pneumonia (Chowdhury et al., 2020) | X-Ray        | Chest                 | 1,345   |
| Radiography-COVID (Chowdhury et al., 2020)           | X-Ray        | Chest                 | 10,844  |
| CDD-CESM (Khaled et al., 2021)                       | X-Ray        | Breast lesion         | 1,233   |
| BreastUS (Vitale et al., 2020)                       | Ultrasound   | Breast lesion         | 1,294   |
| LiverUS (Vitale et al., 2020)                        | Ultrasound   | Liver                 | 39      |
| FH-PS-AOP (Jieyun & ZhanHong, 2024)                  | Ultrasound   | Transperineal         | 8,000   |
| REFUGE (Orlando et al., 2020)                        | Fundus       | Retinal               | 2,400   |
| NeoPolyp (Ngoc Lan et al., 2021)                     | Endoscopy    | Colon polyp           | 2,050   |
| PolypGen (Ali et al., 2023)                          | Endoscopy    | Colon polyp           | 1,411   |
| Total  | 6 Modalities |                       | 419,659 |

## B. Implementation Details

### B.1. Trajectory Construction

To train our model for a multi-step medical image segmentation agent, we require a dataset of expert-like interaction trajectories. We employed an automated algorithm to generate these trajectories by simulating the sequential refinement process an expert annotator would perform. While existing methods (Zhu et al., 2025; Jiang et al., 2026) rely on a rigid point-wise simulation driven by pixel-level discrepancies, they typically restrict the action space to sequential clicks. Such a limitation fails to capture the multi-modal nature of human workflows, where practitioners often initiate segmentation by defining a Bounding Box before refining with precise clicks. To better align with human intuition, we propose a hybrid prompting strategy, as detailed in Algorithm 1. This strategy encompasses both Box-to-Point and Sequential-Click paradigms to generate diverse and realistic interaction trajectories.

---

**Algorithm 1** Hybrid Prompting Strategy for Trajectory Generation

---

**Require:** Image  $I$ , ground truth mask  $M_{\text{target}}$ , state  $s$ , segmentation model  $f_{\theta}$ , max clicks  $K$ , gain threshold  $\tau$ , max retries  $N$

**Ensure:** Trajectory  $\mathcal{T} = \{(a_0, M_0), (a_1, M_1), \dots, (a_T, M_T)\}$

```

1: paradigm  $\leftarrow \{\text{“Box-to-Point”, “Sequential-Click”}\}$ 
2:  $\mathcal{T} \leftarrow \emptyset$ 
3: {Initialization at  $t = 0$  using either Bounding Box or Centroid Click}
4: if paradigm = “Box-to-Point” then
5:    $a_0 \leftarrow \text{ExtractBoundingBox}(M_{\text{target}}) + \epsilon$ , where  $\epsilon \sim \mathcal{U}(-\delta, \delta)$ 
6: else
7:    $a_0 \leftarrow \frac{1}{|M_{\text{target}}|} \sum_{(x,y) \in M_{\text{target}}} (x, y) + \epsilon$ 
8: end if
9:  $M_0 \leftarrow f_{\theta}(I, a_0)$ 
10:  $\mathcal{T} \leftarrow \mathcal{T} \cup \{(a_0, M_0)\}$ 
11: for  $t = 1$  to  $K$  do
12:    $\text{FN}_t \leftarrow M_{\text{target}} \setminus M_{t-1}$ ,  $\text{FP}_t \leftarrow M_{t-1} \setminus M_{\text{target}}$ 
13:   if  $|\text{FN}_t| = 0$  and  $|\text{FP}_t| = 0$  then
14:     break
15:   end if
16:   {Error-driven refinement with retry mechanism}
17:   success  $\leftarrow$  False
18:   for trial = 1 to  $N$  do
19:     if  $|\text{FN}_t| > |\text{FP}_t|$  then
20:        $a_t \leftarrow \arg \max_{p \in \text{FN}_t} \mathcal{D}(p)$  (Positive Click)
21:     else
22:        $a_t \leftarrow \arg \max_{p \in \text{FP}_t} \mathcal{D}(p)$  (Negative Click)
23:     end if
24:      $M_t \leftarrow f_{\theta}(I, s_{t-1})$ 
25:      $\Delta \text{IoU}_t \leftarrow \text{IoU}(M_t, M_{\text{target}}) - \text{IoU}(M_{t-1}, M_{\text{target}})$ 
26:     if  $\Delta \text{IoU}_t \geq \tau$  then
27:        $\mathcal{T} \leftarrow \mathcal{T} \cup \{(a_t, M_t)\}$ 
28:       success  $\leftarrow$  True
29:       break
30:     else
31:       Resample  $a_t$  by selecting alternative local maxima in  $\mathcal{D}(\cdot)$ 
32:     end if
33:   end for
34:   if not success then
35:     break {Early stop if no significant improvement after  $N$  retries}
36:   end if
37: end for
38: return  $\mathcal{T}$ 

```

---

The key innovation of our approach lies in an adaptive error-driven refinement mechanism combined with progress-constrained sampling. Rather than randomly sampling prompts, we leverage morphological analysis of prediction errors. We identify False Negative (FN) regions where the model under-segments and False Positive (FP) regions where it over-segments, then apply distance transforms to localize the most significant error clusters. This ensures that each corrective action addresses the most salient morphological defects. Furthermore, to guarantee trajectory quality, we enforce a constraint where each action must yield a measurable IoU improvement, filtering out ineffective interactions through an iterative retry mechanism. Our trajectory generation strategy differs primarily in the initial prompt  $a_0$ . In the Box-to-Point workflow,  $a_0$  is a bounding box generated by extracting the axis-aligned rectangle of  $M_{\text{target}}$  with a random jitter  $\epsilon \sim \mathcal{U}(-\delta, \delta)$  to simulate human imprecision. In contrast, the Sequential-Click paradigm begins with a point prompt sampled from the centroid of the target mask:

$$a_0 = \frac{1}{|M_{\text{target}}|} \sum_{(x,y) \in M_{\text{target}}} (x, y) + \epsilon \quad (8)$$

Regardless of initialization, all subsequent refinement steps at  $t > 0$  follow a unified error-driven mechanism. The agent analyzes the prediction error  $E_t = M_{\text{pred}}^{(t)} \oplus M_{\text{target}}$ , decomposed into  $\text{FN}_t = M_{\text{target}} \setminus M_{\text{pred}}^{(t)}$  and  $\text{FP}_t = M_{\text{pred}}^{(t)} \setminus M_{\text{target}}$ . By applying a distance transform  $\mathcal{D}(\cdot)$ , we identify the centroids of the largest error components. Corrective clicks are sampled as:

$$a_t = \begin{cases} \arg \max_{p \in \text{FN}_t} \mathcal{D}(p), & \text{if } |\text{FN}_t| > |\text{FP}_t| \\ \arg \max_{p \in \text{FP}_t} \mathcal{D}(p), & \text{otherwise} \end{cases} \quad (9)$$

with positive labels for FN clicks and negative labels for FP clicks. To ensure the efficiency of synthesized trajectories, we implement a progress-constrained sampling mechanism. We require each simulated action to yield an incremental IoU gain ( $\Delta \text{IoU}$ ) exceeding a predefined threshold  $\tau$ :

$$\Delta \text{IoU}_t = \text{IoU}(M_t, M_{\text{target}}) - \text{IoU}(M_{t-1}, M_{\text{target}}) \geq \tau \quad (10)$$

where  $\tau$  is typically set to 0.04. If a candidate action fails to satisfy this threshold, the simulator performs iterative resampling up to  $N$  trials (default  $N = 5$ ) to identify a more constructive interaction. During each retry, we re-sample the click position within the error region by selecting alternative local maxima in the distance transform map or introducing controlled perturbations. If no valid action is found after  $N$  trials, the trajectory generation is terminated early. This validation process ensures that the trajectory dataset  $\mathcal{D}_{\text{traj}}$  is composed of high-quality, monotonically improving sequences. We set  $K = 5$  as the maximum number of refinement clicks,  $\tau = 0.04$  as the gain threshold, and  $N = 5$  as the maximum retry attempts. Bounding box jitter is sampled from  $\mathcal{U}(-5, 5)$  pixels, while click jitter follows  $\mathcal{N}(0, 2^2)$  pixels. The generated trajectories are stored in JSON format, recording each action  $a_t$ , intermediate mask  $M_t$ .

Our implementation leverages MedSAM2 (Ma et al., 2025b) and IMISNet (Cheng et al., 2025) as the base segmentation models  $f_\theta$ . Based on this trajectory generation pipeline, we initially generated 334,616 trajectories for both the Box-to-Point and Sequential-Click strategies using MedSAM2. To ensure the quality of the Supervised Fine-Tuning (SFT) data, we applied an IoU threshold of 0.7 to filter out low-performing samples. This resulted in 188,687 click-based and 260,446 box-based trajectories, totaling 449,133 high-quality samples. A similar procedure was applied using IMISNet, yielding 235,993 click trajectories and 283,522 box trajectories, for a total of 519,515 samples. These filtered trajectories served as the SFT data to train their respective models.

## B.2. Prompt Design

The reasoning capabilities of MedSAM-Agent are governed by a structured system prompt that defines the agent’s role, tool-use protocols, and decision-making heuristics. This prompt ensures that the MLLM interprets the medical image not as a static object, but as a dynamic environment requiring strategic intervention.

### B.2.1. TOOL SPECIFICATIONS

We provide the agent with a rigorous schema for tool calling. Specifically, the model is instructed to output its decisions in a standard JSON format, selecting from `add_box`, `add_point`, or `stop_action`. To maintain procedural clarity, the system prompt enforces a “Single Action per Turn” rule, requiring the model to observe the visual feedback from the segmentation backend before initiating the subsequent refinement step.

### B.2.2. SYSTEM PROMPT

As for the system prompt, we first initialize the model as a professional segmentation annotator, grounding its objective in high-precision clinical mask creation. The prompt explicitly informs the agent that the mask is rendered as a “semi-transparent green overlay”, enabling the model to visually contrast the current prediction with the underlying anatomy to identify areas requiring refinement.

## Functional Tools (json)

```
[
  {
    "type": "function",
    "function": {
      "name": "add_bbox",
      "description": "Add a bounding box to initialize or refine the segmentation.",
      "parameters": {
        "type": "object",
        "properties": {
          "bbox_2d": { "type": "array", "items": { "type": "integer"}, "minItems": 4, "maxItems": 4, "description": "2D bounding box in [x1, y1, x2, y2] format" }
        },
        "required": ["bbox_2d"]
      }
    }
  },
  {
    "type": "function",
    "function": {
      "name": "add_point",
      "description": "Add a point to refine the mask (positive to include areas, negative to exclude areas.)",
      "parameters": {
        "type": "object",
        "properties": {
          "point_2d": { "type": "array", "items": { "type": "integer"}, "minItems": 2, "maxItems": 2, "description": "2D coordinate point in [x, y] format" },
          "point_type": { "type": "string", "enum": ["positive", "negative"] }
        },
        "required": ["point_2d", "point_type"]
      }
    }
  },
  {
    "type": "function",
    "function": {
      "name": "stop_action",
      "description": "Stop the refinement process when the mask accurately covers the target object.",
      "parameters": { "type": "object", "properties": {} }
    }
  }
]
```

## System Prompt

You are a professional segmentation annotator specializing in mask creation and refinement. Your core task is to segment the **USER-SPECIFIED TARGET REGION** from the provided image. No preliminary mask is available—you must first create an initial mask using the tool, then iteratively refine it to achieve pixel-level accuracy. The mask will be displayed as a semi-transparent green overlay; your goal is to ensure it exactly covers the entire target region and excludes all non-target areas (e.g., background, adjacent objects).

## # Tools

You must call one function to assist with the user query. You are provided with function signatures within `<tools></tools>` XML tags:

`<tools>`

*[The JSON-formatted tool signatures are inserted here]*

`</tools>`

For each function call, return a json object with function name and arguments within `<tool_call></tool_call>` XML tags:

```
<tool_call>
{"name": <function-name>, "arguments": <args-json-object>}
</tool_call>
```

Only use the provided functions to complete your task. Do not invent or assume any other functions. Carefully consider the current mask state before each action.

### B.2.3. INTERACTION PROTOCOL

The interaction protocol is structured as a closed-loop dialogue that transitions from initial localization to iterative refinement, mimicking a clinical workflow. The process begins with an initialization turn, where the agent receives the target specification and performs the first localization action. This is followed by subsequent refinement turns, during which the agent evaluates the visual feedback of the mask overlay against the anatomical structure, strategically placing positive or negative points to correct errors. The cycle continues until the agent, guided by its internal reward-optimized policy, determines that the segmentation has reached pixel-level accuracy and invokes the termination action to finalize the task efficiently.

#### Initial Turn prompt

`<image>` The target to be segmented is: **{target\_description}**.  
Now, please analyze the original image, then decide your first action.

#### Subsequent Turns prompt

`<image>` Here is the updated mask after your previous action. Based on this, what is your next action? If the mask is now accurate, you can call '**stop\_action**' to finish.

Based on these prompts, we format the resulting interaction sequences into a standard Supervised Fine-Tuning (SFT) data structure to facilitate the model's cold-start training.

## B.3. Training Details

The resolution of all datasets in our experiments is  $1024 \times 1024$ . During the construction of interaction trajectories, we map the spatial coordinates to absolute integers within a  $[0, 1000]$  range to ensure compatibility with the Qwen3-VL (Bai et al., 2025) architecture. This normalization enables the model to effectively process spatial prompts and achieve high-precision interactive segmentation.

During the SFT stage, we utilize the Llama-Factory (Zheng et al., 2024b) framework with a learning rate of  $1 \times 10^{-5}$  and a total batch size of 64. The number of training epochs is 4. To maintain training efficiency and leverage pre-trained visual representations, we only update the parameters of the LLM backbone, while keeping the vision encoder and projector frozen. The training is accelerated using the DeepSpeed ZeRO-3 strategy.

The RL stage is implemented via the Verl framework (Sheng et al., 2024), using a learning rate of  $1 \times 10^{-5}$ , a batch size of 8, and a sampling size of 8 per prompt. The maximum interaction depth is set to 5 turns. To maximize training throughput, we employ an asynchronous multi-turn sampling mechanism integrated with the SGLang (Zheng et al., 2024a) runtime, enabling efficient concurrent inference during the policy rollout phase. As for the hyper-parameters, we set  $w_{iou} = w_{dice} = 0.5$ ,  $w_1 = 0.2$ ,  $w_2 = 0.8$ ,  $\lambda_1 = 0.1$ ,  $\lambda_2 = 1.0$ , and  $\lambda_3 = 0.01$ . All experiments were conducted on  $8 \times$  NVIDIA H20 (96G) GPUs.

During the RL stage, given that medical segmentation requires a rigorous focus on fine-grained visual details, we deviate from the conventional reasoning-agent setup by omitting a dedicated `<think>` token. This design choice is driven by two primary objectives: first, to significantly accelerate inference speed by reducing token overhead; and second, to force the model to prioritize dense image-level features over textual deliberation. By bypassing the explicit thinking step, we encourage the agent to internalize spatial reasoning directly within its action space, ensuring that its decision-making is more tightly coupled with the immediate morphological characteristics of the lesion.

## C. Experiments Results

### C.1. Comparison Experiment

In our experiments, we compare our method with representative interactive segmentation frameworks, including the general-purpose SAM2 (Ravi et al., 2024) and domain-specific models such as MedSAM2 (Ma et al., 2025b) and IMISNet (Cheng et al., 2025). For these baselines, we report results using both *Point* and *Box* prompts. “Point” results are generated using the center of the ground-truth mask, while “Box” results utilize corresponding bounding boxes. The *Box* prompt performance is generally regarded as the empirical upper bound for single-turn interactive segmentation. Furthermore, we benchmark against SOTA MLLM-based methods, including four general-domain models (LISA (Lai et al., 2024), GALLM (Rasheed et al., 2024), HyperSeg (Wei et al., 2024a), and Seg-R1 (You & Wu, 2025)) and three specialized medical MLLMs (MedPLIB (Huang et al., 2025b), UniBioMed (Wu et al., 2025b), and Citrus-V (Wang et al., 2025a)).

Table 5 and Table 6 demonstrate all results of 21 datasets across 6 medical modalities. The empirical results reveal that the performance of our autonomous agent is intrinsically linked to the foundational capabilities of the underlying segmentation model, yet it demonstrates a unique capacity to improve upon baseline results through strategic interaction. For instance, while specialized models like IMISNet demonstrate exceptional proficiency in CT datasets, their performance significantly decreases when applied to X-Ray, as observed in the Radiography (Chowdhury et al., 2020) results. However, our multi-turn agentic framework addresses these limitations by iteratively identifying residual errors and applying corrective logic. By engaging in multiple rounds of interaction, the agent achieves performance that surpasses the inherent limits of a single-turn approach, thereby demonstrating the fundamental significance of multi-turn strategic engagement. This phenomenon suggests that MedSAM-Agent has internalized a sophisticated refinement logic that goes beyond simple tool invocation. By evaluating the segmentation state at each turn, the agent autonomously decides on corrective measures to eliminate hallucinations and under-segmentation. This active perception allows the agent to enhance raw model capabilities to reach the high precision required for clinical diagnostics, proving that autonomous, multi-turn strategic interaction is superior to passive, single-turn prompting paradigms.

### C.2. Case Study

In this section, we provide qualitative examples of MedSAM-Agent across various medical imaging modalities to demonstrate its interactive reasoning capabilities (Fig. 4). Unlike traditional single-turn models, our agent engages in a multi-step refinement process, iteratively evaluating the current segmentation mask and adjusting its strategy based on visual feedback. In these visualizations, yellow prompts indicate positive clicks or bounding boxes used to define the target anatomy, while red prompts represent negative clicks deployed to exclude false-positive regions or refine over-segmented boundaries.

As shown in the sequential turns, MedSAM-Agent typically initiates the process with a global constraint and subsequently applies local corrective measures to eliminate hallucinations and fill in under-segmented areas. This autonomous refinement loop effectively mimics a clinician’s iterative workflow, proving that the model can successfully internalize sophisticated decision heuristics to achieve superior mask fidelity in challenging clinical environments.

## D. Future Works

In future research, we plan to extend the MedSAM-Agent framework along the following three strategic dimensions:

**Expansion to Volumetric Modalities.** While the current study focuses on 2D image slices, many clinical diagnostic tasks rely on 3D volumetric data, such as CT and MRI scans. We aim to extend the agent’s action space and reinforcement learning environment to handle 3D spatial contexts. This transition will enable the agent to capture cross-slice anatomical continuity, providing more consistent and clinically accurate volumetric segmentations.

**Development of a Unified multi-modal Agent.** While our work focuses on the specialized task of interactive segmentation, the proposed autonomous decision-making framework is inherently extensible. In the future, we intend to evolve MedSAM-Agent into a unified medical AI assistant capable of performing diverse medical imaging tasks (e.g., Medical VQA, lesion classification, and automated report generation) within a single, cohesive architecture. By treating these distinct tasks as specialized tool-use actions, we can integrate new capabilities without altering the core agentic framework. This evolution aims to provide a comprehensive assistant that supports the entire clinical workflow, seamlessly transitioning between perception, reasoning, and high-precision interaction.

**Enhancement of Computational Efficiency.** A potential limitation of multi-turn iterative paradigms is the increased

cumulative latency during inference. In future work, we plan to explore more efficient architectures and sampling strategies to mitigate this overhead. Specifically, we will investigate the integration of early-exit mechanisms to terminate redundant computation when high-confidence masks are achieved and leverage speculative decoding or KV-cache optimization techniques tailored for multi-modal agents. These advancements will ensure that the superior precision of MedSAM-Agent is delivered with the near-real-time responsiveness required for high-throughput clinical applications.

**Table 5. Quantitative comparison across CT, MRI, and Endoscopy.** Point and Box denote the interactive prompts derived from the ground-truth center points and bounding boxes, respectively, which are utilized to evaluate the single-round segmentation performance. **Bold** and underlined values represent the best and second-best performance among non-interactive methods, respectively.

|               |  | CT      |              |              |              |              |              | MRI          |              |              | Endoscopy    |              |              |
|---------------|--|---------|--------------|--------------|--------------|--------------|--------------|--------------|--------------|--------------|--------------|--------------|--------------|
|               |  | Flare22 |              |              | KiTS         | LIDC-IDRI    | BTCV         | amos-CT      | WORD         | ACDC         | LGG          | amos-MRI     | NeoPolyp     |
|               |  | Dice    | 0.766        | 0.666        | 0.508        | 0.634        | 0.601        | 0.487        | 0.532        | 0.439        | 0.492        | 0.641        | 0.678        |
| SAM2-Point    |  | IoU     | 0.697        | 0.563        | 0.430        | 0.564        | 0.529        | 0.405        | 0.446        | 0.354        | 0.436        | 0.585        | 0.608        |
| SAM2-Box      |  | Dice    | 0.920        | 0.818        | 0.756        | 0.890        | 0.869        | 0.772        | 0.809        | 0.865        | 0.839        | 0.934        | 0.911        |
| SAM2-Box      |  | IoU     | 0.863        | 0.720        | 0.648        | 0.821        | 0.796        | 0.674        | 0.718        | 0.775        | 0.752        | 0.887        | 0.856        |
| MedSAM-Point  |  | Dice    | 0.831        | 0.655        | 0.763        | 0.795        | 0.751        | 0.686        | 0.556        | 0.869        | 0.577        | 0.844        | 0.800        |
| MedSAM-Point  |  | IoU     | 0.746        | 0.528        | 0.645        | 0.700        | 0.660        | 0.558        | 0.498        | 0.779        | 0.476        | 0.762        | 0.711        |
| MedSAM-Box    |  | Dice    | 0.913        | 0.836        | 0.773        | 0.890        | 0.888        | 0.781        | 0.847        | 0.893        | 0.821        | 0.933        | 0.916        |
| MedSAM-Box    |  | IoU     | 0.847        | 0.735        | 0.668        | 0.815        | 0.814        | 0.674        | 0.766        | 0.813        | 0.725        | 0.884        | 0.859        |
| IMISNet-Point |  | Dice    | 0.845        | 0.677        | 0.268        | 0.819        | 0.745        | 0.692        | 0.753        | 0.622        | 0.660        | 0.798        | 0.764        |
| IMISNet-Point |  | IoU     | 0.766        | 0.554        | 0.221        | 0.725        | 0.638        | 0.577        | 0.634        | 0.485        | 0.548        | 0.704        | 0.659        |
| IMISNet-Box   |  | Dice    | 0.911        | 0.826        | 0.524        | 0.870        | 0.869        | 0.829        | 0.857        | 0.860        | 0.830        | 0.924        | 0.885        |
| IMISNet-Box   |  | IoU     | 0.852        | 0.740        | 0.443        | 0.797        | 0.794        | 0.736        | 0.767        | 0.766        | 0.741        | 0.871        | 0.821        |
| LISA          |  | Dice    | 0.116        | 0.147        | 0.006        | 0.062        | 0.097        | 0.098        | 0.069        | 0.185        | 0.076        | 0.271        | 0.293        |
| LISA          |  | IoU     | 0.070        | 0.086        | 0.003        | 0.036        | 0.057        | 0.055        | 0.037        | 0.107        | 0.044        | 0.220        | 0.225        |
| GLAMM         |  | Dice    | 0.128        | 0.110        | 0.005        | 0.078        | 0.106        | 0.103        | 0.050        | 0.188        | 0.078        | 0.204        | 0.285        |
| GLAMM         |  | IoU     | 0.079        | 0.061        | 0.003        | 0.048        | 0.066        | 0.059        | 0.027        | 0.109        | 0.046        | 0.149        | 0.208        |
| HyperSeg      |  | Dice    | 0.117        | 0.175        | 0.006        | 0.068        | 0.099        | 0.121        | 0.160        | 0.183        | 0.117        | 0.392        | 0.400        |
| HyperSeg      |  | IoU     | 0.089        | 0.129        | 0.003        | 0.046        | 0.067        | 0.078        | 0.102        | 0.119        | 0.083        | 0.344        | 0.341        |
| Seg-R1        |  | Dice    | 0.113        | 0.159        | 0.009        | 0.087        | 0.102        | 0.124        | 0.134        | 0.168        | 0.076        | 0.515        | 0.551        |
| Seg-R1        |  | IoU     | 0.080        | 0.104        | 0.005        | 0.055        | 0.064        | 0.076        | 0.081        | 0.098        | 0.045        | 0.457        | 0.485        |
| MedPLIB       |  | Dice    | 0.046        | 0.033        | 0.001        | 0.083        | 0.054        | 0.096        | 0.118        | 0.318        | 0.096        | 0.123        | 0.142        |
| MedPLIB       |  | IoU     | 0.035        | 0.021        | 0.001        | 0.058        | 0.038        | 0.075        | 0.088        | 0.252        | 0.070        | 0.092        | 0.102        |
| UniBiomed     |  | Dice    | 0.825        | 0.755        | 0.502        | 0.735        | 0.822        | 0.707        | 0.827        | <b>0.863</b> | <b>0.732</b> | <b>0.851</b> | 0.705        |
| UniBiomed     |  | IoU     | 0.747        | 0.670        | 0.405        | 0.646        | 0.738        | 0.599        | 0.738        | <b>0.776</b> | <b>0.635</b> | <b>0.784</b> | 0.623        |
| Citrus-V      |  | Dice    | 0.480        | 0.470        | 0.221        | 0.428        | 0.262        | 0.314        | 0.438        | 0.305        | 0.235        | 0.549        | 0.783        |
| Citrus-V      |  | IoU     | 0.417        | 0.377        | 0.170        | 0.370        | 0.220        | 0.258        | 0.326        | 0.254        | 0.194        | 0.510        | 0.722        |
| Ours-IMISNet  |  | Dice    | <b>0.848</b> | <b>0.791</b> | 0.406        | <b>0.780</b> | <b>0.828</b> | <b>0.741</b> | <b>0.836</b> | 0.828        | 0.685        | 0.813        | 0.793        |
| Ours-IMISNet  |  | IoU     | <b>0.779</b> | <b>0.710</b> | 0.340        | <b>0.702</b> | <b>0.751</b> | <b>0.642</b> | <b>0.743</b> | 0.728        | 0.583        | 0.753        | 0.719        |
| Ours-MedSAM2  |  | Dice    | 0.836        | 0.703        | <b>0.523</b> | 0.773        | 0.805        | 0.681        | 0.816        | 0.844        | 0.719        | 0.814        | <b>0.809</b> |
| Ours-MedSAM2  |  | IoU     | 0.761        | 0.597        | <b>0.448</b> | 0.690        | 0.723        | 0.579        | 0.726        | 0.755        | 0.623        | 0.753        | <b>0.735</b> |

**Table 6. Quantitative comparison across X-Ray, Ultrasound, and Fundus.** Point and Box denote the interactive prompts derived from the ground-truth center points and bounding boxes, respectively, which are utilized to evaluate the single-round segmentation performance. **Bold** and underlined values represent the best and second-best performance among non-interactive methods, respectively.

|               |  | X-Ray  |              |              |              |              | Ultrasound   |              |              | Fundus       |              |              |
|---------------|--|--|--------------|--------------|--------------|--------------|--------------|--------------|--------------|--------------|--------------|--------------|
|               |  | CXRMask Rad-LO Rad-N Rad-VP Rad-COVID CDD-CESM |              |              |              |              | BreastUS     | LiverUS      | FH-PS-AOP    | REFUGE       |              |              |
|               |  | Dice   | 0.647        | 0.546        | 0.627        | 0.536        | 0.582        | 0.339        | 0.685        | 0.557        | 0.341        | 0.362        |
| SAM2-Point    |  | IoU  | 0.533        | 0.409        | 0.499        | 0.392        | 0.454        | 0.246        | 0.582        | 0.424        | 0.217        | 0.265        |
| SAM2-Box      |  | Dice   | 0.940        | 0.790        | 0.928        | 0.783        | 0.890        | 0.628        | 0.889        | 0.849        | 0.876        | 0.717        |
| SAM2-Box      |  | IoU  | 0.890        | 0.667        | 0.869        | 0.667        | 0.809        | 0.497        | 0.811        | 0.745        | 0.782        | 0.574        |
| MedSAM-Point  |  | Dice   | 0.887        | 0.878        | 0.956        | 0.922        | 0.941        | 0.477        | 0.808        | 0.421        | 0.543        | 0.414        |
| MedSAM-Point  |  | IoU  | 0.828        | 0.796        | 0.919        | 0.861        | 0.894        | 0.360        | 0.711        | 0.286        | 0.405        | 0.346        |
| MedSAM-Box    |  | Dice   | 0.946        | 0.912        | 0.976        | 0.903        | 0.955        | 0.692        | 0.918        | 0.856        | 0.896        | 0.846        |
| MedSAM-Box    |  | IoU  | 0.899        | 0.842        | 0.953        | 0.832        | 0.918        | 0.572        | 0.851        | 0.752        | 0.815        | 0.743        |
| IMISNet-Point |  | Dice   | 0.719        | 0.444        | 0.764        | 0.462        | 0.694        | 0.386        | 0.726        | 0.257        | 0.483        | 0.677        |
| IMISNet-Point |  | IoU  | 0.590        | 0.304        | 0.647        | 0.316        | 0.564        | 0.271        | 0.607        | 0.171        | 0.335        | 0.528        |
| IMISNet-Box   |  | Dice   | 0.948        | 0.639        | 0.916        | 0.465        | 0.838        | 0.430        | 0.873        | 0.209        | 0.625        | 0.841        |
| IMISNet-Box   |  | IoU  | 0.901        | 0.535        | 0.859        | 0.368        | 0.757        | 0.349        | 0.791        | 0.148        | 0.509        | 0.733        |
| LISA          |  | Dice   | 0.243        | 0.621        | 0.220        | 0.487        | 0.187        | 0.177        | 0.218        | 0.615        | 0.321        | 0.036        |
| LISA          |  | IoU  | 0.184        | 0.469        | 0.163        | 0.325        | 0.126        | 0.111        | 0.147        | 0.466        | 0.227        | 0.019        |
| GLAMM         |  | Dice   | 0.192        | 0.504        | 0.178        | 0.473        | 0.173        | 0.190        | 0.315        | 0.611        | 0.282        | 0.027        |
| GLAMM         |  | IoU  | 0.136        | 0.344        | 0.121        | 0.325        | 0.117        | 0.121        | 0.231        | 0.463        | 0.189        | 0.014        |
| HyperSeg      |  | Dice   | 0.329        | 0.413        | 0.330        | 0.463        | 0.323        | 0.157        | 0.536        | 0.609        | 0.157        | 0.023        |
| HyperSeg      |  | IoU  | 0.239        | 0.266        | 0.246        | 0.305        | 0.227        | 0.103        | 0.450        | 0.458        | 0.100        | 0.012        |
| Seg-R1        |  | Dice   | 0.446        | 0.583        | 0.383        | 0.522        | 0.385        | 0.186        | 0.625        | 0.613        | 0.233        | 0.455        |
| Seg-R1        |  | IoU  | 0.342        | 0.445        | 0.312        | 0.372        | 0.313        | 0.121        | 0.521        | 0.463        | 0.162        | 0.325        |
| MedPlib       |  | Dice   | 0.225        | 0.086        | 0.076        | 0.030        | 0.156        | 0.116        | 0.135        | 0.088        | 0.042        | 0.297        |
| MedPlib       |  | IoU  | 0.154        | 0.049        | 0.048        | 0.017        | 0.106        | 0.073        | 0.098        | 0.048        | 0.023        | 0.201        |
| UniBiomed     |  | Dice   | 0.936        | 0.887        | 0.959        | 0.871        | 0.894        | 0.357        | <b>0.828</b> | 0.620        | 0.761        | 0.794        |
| UniBiomed     |  | IoU  | 0.885        | 0.804        | 0.923        | 0.782        | 0.830        | 0.262        | <b>0.743</b> | 0.470        | 0.640        | 0.668        |
| Citrus-V      |  | Dice   | 0.694        | 0.702        | 0.713        | 0.799        | 0.653        | 0.186        | 0.324        | 0.040        | 0.038        | 0.782        |
| Citrus-V      |  | IoU  | 0.601        | 0.600        | 0.623        | 0.716        | 0.542        | 0.136        | 0.237        | 0.021        | 0.022        | 0.655        |
| Ours-IMISNet  |  | Dice   | <b>0.947</b> | 0.832        | 0.941        | 0.843        | 0.902        | 0.324        | 0.788        | 0.432        | 0.756        | 0.803        |
| Ours-IMISNet  |  | IoU  | <b>0.899</b> | 0.729        | 0.892        | 0.747        | 0.829        | 0.242        | 0.699        | 0.294        | 0.641        | 0.678        |
| Ours-MedSAM2  |  | Dice   | 0.930        | <b>0.900</b> | <b>0.973</b> | <b>0.874</b> | <b>0.948</b> | <b>0.375</b> | 0.805        | <b>0.777</b> | <b>0.798</b> | <b>0.813</b> |
| Ours-MedSAM2  |  | IoU  | 0.876        | <b>0.828</b> | <b>0.950</b> | <b>0.796</b> | <b>0.906</b> | <b>0.291</b> | 0.719        | <b>0.647</b> | <b>0.689</b> | <b>0.692</b> |

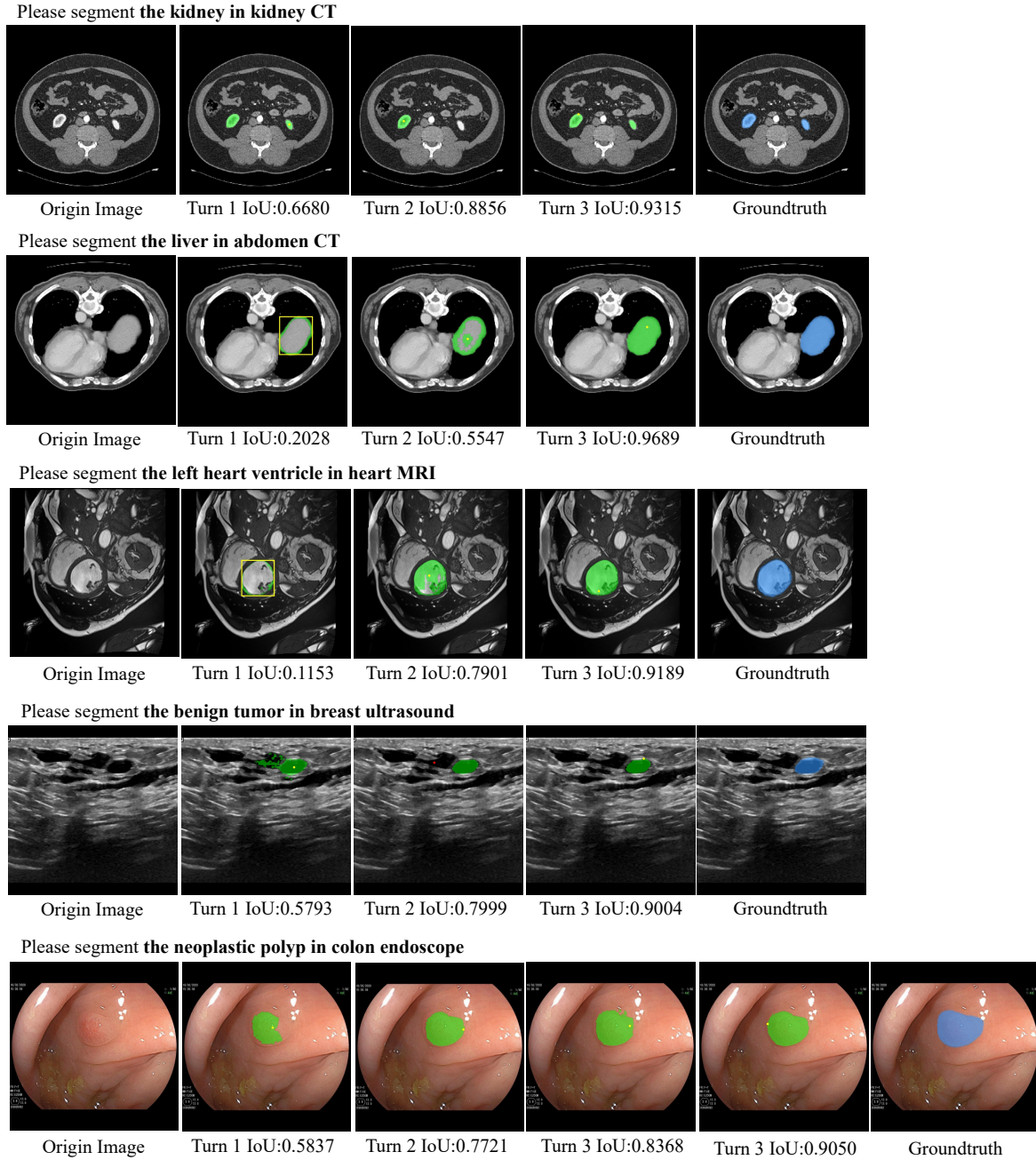


Figure 4. Case study. Yellow boxes indicate bounding box prompts, yellow points represent positive clicks, and red points denote negative clicks.